Petroleum Science 22 (2025) 193–209

Contents lists available at ScienceDirect

Petroleum Science

journal homepage: www.keaipublishing.com/en/journals/petroleum-science

Original Paper

Characterization of petrophysical and seismic properties for CO_2 storage with sensitivity analysis

Yan-Jiao Dong [a, b], Yi Shen [b, *], Kai Guo [a, c], Xiao-Qin Wu [b], Qiang Mao [b], Wen-Yue Sun [d], Zhi-Qiang Wang [d]

[a] State Key Laboratory of Offshore Oil and Gas Exploitation, Beijing, 100028, China
[b] Geosciences Department, China University of Petroleum (East China), Qingdao, 266580, Shandong, China
[c] CNOOC Research Institute Ltd., Beijing, 100028, China
[d] School of Petroleum Engineering, China University of Petroleum (East China), Qingdao, 266580, Shandong, China

ARTICLE INFO

Article history:
Received 23 January 2024
Received in revised form
29 May 2024
Accepted 8 July 2024
Available online 9 July 2024

Edited by Meng-Jiao Zhou

Keywords:
CO_2 storage
Time-lapse seismic
CO_2 plume
Sensitivity analysis
Rock physics
Reservoir simulation
Saline aquifer

ABSTRACT

Saline aquifers are considered as highly favored reservoirs for CO_2 sequestration due to their favorable properties. Understanding the impact of saline aquifer properties on the migration and distribution of CO_2 plume is crucial. This study focuses on four key parameters—permeability, porosity, formation pressure, and temperature—to characterize the reservoir and analyse the petrophysical and elastic response of CO_2. First, we performed reservoir simulations to simulate CO_2 saturation, using multiple sets of these four parameters to examine their significance on CO_2 saturation and the plume migration speed. Subsequently, the effect of these parameters on the elastic properties is tested using rock physics theory. We established a relationship of compressional wave velocity (V_p) and quality factor (Q_p) with the four key parameters, and conducted a sensitivity analysis to test their sensitivity to V_p and Q_p. Finally, we utilized visco-acoustic wave equation simulated time-lapse seismic data based on the computed V_p and Q_p models, and analysed the impact of CO_2 saturation changes on seismic data. As for the above numerical simulations and analysis, we conducted sensitivity analysis using both homogeneous and heterogeneous models. Consistent results are found between homogeneous and heterogeneous models. The permeability is the most sensitive parameter to the CO_2 saturation, while porosity emerges as the primary factor affecting both Q_p and V_p. Both Q_p and V_p increase with the porosity, which contradicts the observations in gas reservoirs. The seismic simulations highlight significant variations in the seismic response to different parameters. We provided analysis for these observations, which serves as a valuable reference for comprehensive CO_2 integrity analysis, time-lapse monitoring, injection planning and site selection.

* Corresponding author.
E-mail address: yishen@upc.edu.cn (Y. Shen).

https://doi.org/10.1016/j.petsci.2024.07.011

Nomenclature

Sg_i	The saturation of CO_2 in the i grid	M_0	The compression modulus at an extremely low frequency, GPa
$Q_{P_{max}}^{-1}$	The maximum inverse quality factor of the P-wave	M_∞	The compression modulus at an extremely high frequency, GPa
ϕ	Porosity	M_S	The compression modulus of mineral matrix, GPa
K_f	The effective bulk modulus of the fluid in a rock, GPa	M_{Dry}	The compression modulus of rock skeleton, Pa
M_G	The compressional modulus of CO_2-only rock, GPa	M_W	The compressional modulus of wet rock, GPa
K_g	The bulk modulus of CO_2, GPa	K_W	The bulk modulus of water, GPa
V_p	The P-wave velocity, m/s	S_W	The water saturation
v_0	The initial P-wave velocity, m/s	ρ	The volume density, kg/m^3
p	The acoustic pressure, GPa	γ	Dimensionless variable
n	The number of grids		

1. Introduction

Over the past few decades, geological sequestration had been widely recognized as a highly effective method for reducing CO_2 emissions and stabilizing greenhouse gas concentrations in the atmosphere. During the CO_2 injection phase, buoyancy caused the gas to move upwards (Dai et al., 2014). The migration of supercritical CO_2 was captured by three main mechanisms: hydrodynamic capture, solution capture, and mineral capture (Bachu et al., 1994; Gershenzon et al., 2015; Iglauer et al., 2015; Xu et al., 2004). Various types of storage sites could be utilized for CO_2 storage, including deep saline aquifers (Bourne et al., 2014; Rutqvist et al., 2010), depleted gas reservoirs (Orlic, 2016; Raza et al., 2018), abandoned coal seams (Bachu, 2007), deep-sea locations, and basalt formations. Among the listed sequestration sites, deep saline aquifers are considered highly favorable reservoirs. Their advantages include broad distribution, substantial storage capacities up to tens of billions of tons, relatively high security, and a relatively mature level of commercial technology (Metz et al., 2005). Therefore, it is crucial to enhance our understanding of saline aquifer properties and characteristics to simulate CO_2 sequestration accurately and conduct 4D seismic monitoring. 4D seismic monitoring technology is now widely used in many CO_2 enhanced oil recovery (EOR) projects worldwide. This method plays a crucial role as CO_2 storage associated with EOR constitutes the largest volume of stored CO_2 (Barajas-Olalde et al., 2021; Jin et al., 2021; Mur et al., 2020). Typically, most researchers primarily concentrate on analysing the sensitivity of geological environmental factors and CO_2 injection parameters to the post-CO_2 injection formation.

On the one hand, it is important to perform reservoir modeling and analyse the sensitivity of CO_2 saturation to different factors to characterize the aquifer, and to evaluate the impact of the geological environment and aquifer properties on CO_2 storage. At present, many scholars have conducted studies on the sensitivity of saline aquifers following CO_2 injection. Zhu et al. (2015) found that the range of the simulated plume was significantly influenced by permeability anisotropy, temperature, and CH_4, while showing less sensitivity to other parameters. Xiao et al. (2018) conducted a single-factor analysis, revealing that bottom-hole pressure and fracture permeability significantly impacted production. However, they did not address CO_2 injection parameters in their study. Wiese et al. (2010) conducted sensitivity analysis on input parameters and revealed that aquifer permeability and thickness had a dominant influence. These studies highlight the importance of understanding the sensitivity of various factors in CO_2 sequestration within saline aquifers.

On the other hand, extensive monitoring plays an important role in understanding and verifying the long-term integrity and effectiveness of the saline aquifer for CO_2 storage (Lackner, 2003). Time-lapsed (or ″4D″) seismic events offer a reliable method for large-scale fluid monitoring, particularly in validating trap integrity throughout the lifecycle of a project (Lumley, 2010). Widely utilized for decades in the oil and gas industry, this method detects hydrocarbons through time-lapse monitoring and effectively monitors fluid movement in underground reservoirs (Johnston, 2013; Will et al., 2021). Recently, most carbon capture utilization and storage (CCUS) initiatives have employed time-lapse methods to monitor the transport and distribution of CO_2 underground. Specifically, seismic methods are frequently used for short-term or long-term monitoring of CO_2 storage (Arts et al., 2004; Kazemeini et al., 2010; Tanase and Tanaka, 2021; Zhu et al., 2017). Time-lapse seismic monitoring is cost-effective, especially for offshore storage projects, and has demonstrated its effectiveness in monitoring subsurface CO_2 dynamics (Ajo-Franklin et al., 2013; Lazaratos and Marion, 1997). For example, this technique has been applied in various locations including Sleipner in Norway-North Sea (Arts et al., 2004; Li and Li, 2021), Snøhvit in Norway-Barents Sea (Eiken et al., 2011), Tomakomai offshore Hokkaido Islands (Tanase and Tanaka, 2021), In Salah (Mathieson et al., 2010), Weyburn (Davis et al., 2003; White, 2013), Ketzin onshore Germany (Kazemeini et al., 2010), and the United States Department of Energy Illinois Basin sequestration pilot (Couëslan et al., 2014). These examples highlight the effectiveness and widespread application of time-lapse seismic imaging in monitoring CO_2 storage in various locations.

Notably, the injected CO_2 into formations has significant effects on the fluid systems within the reservoir. This injection cause various changes, including changes in fluid saturation, pore pressure, fluid density, and the sealing capacity of the cap layer. Consequently, the injection of CO_2 modifies the elastic characteristics of the reservoir. This affects seismic velocity and attenuation, thereby impacting the propagation of seismic waves (Carcione et al., 2006; Leong et al., 2022). In return, the discernible changes in P-wave amplitude or travel time comprehensively reflects CO_2 saturation and pore pressure. For example, at Sleipner, time-lapse seismic monitoring quantitively describes the distribution of CO_2 in strata. It analyses alterations in seismic wave velocity and attenuation before and after gas injection (Chadwick et al., 2019; Zhu et al., 2017). Therefore, V_p and Q_p are two key seismic parameters that represents the seismic response to the CO_2 saturation.

Previously, Shen et al. (2018c) explored natural gas studies and discovered the significant impact of porosity on P-wave velocity and attenuation, with Q_p and V_p are sensitive to variations in rock properties. However, the sensitivity of injection parameters during CO_2 sequestration in reservoir simulation to Q_p and V_p has not yet been studied. Additionally, our understanding of how aquifer properties and its geological environment impact seismic data for CO_2 storage in deep saline aquifers is limited. In this paper, our goal is to establish a relationship between the aquifer characteristics and the seismic elastic V_p and Q_p. This will help bridge the gap between reservoir modeling and time-lapse seismic monitoring, facilitating a comprehensive understanding of CO_2 plume migration. We characterize the aquifer using reservoir parameters such

as permeability, porosity, formation pressure, and temperature, and explore their relationship to V_p and Q_p. Consequently, we analyse the seismic responses to reservoir properties and CO_2 plume distribution. This study aims to provide a reliable reference for CO_2 integrity analysis, time-lapse monitoring, injection planning, and site selection.

In our paper, we first perform reservoir simulations to analyse the sensitivity of the following influencing parameters to CO_2 saturation post-injection: permeability, porosity, formation pressure, and temperature. Subsequently, we establish a relationship between these four key parameters and the seismic properties of V_p and Q_p, using rock physics theory, with a sensitivity analysis. Finally, we generate the time-lapse seismic data based on the computed V_p and Q_p using the visco-acoustic wave equation. Through the workflow, we integrate the reservoir modeling and seismic modeling to investigate how the saline aquifer influences the seismic properties and seismic response for CO_2 storage.

2. Methodology

2.1. Reservoir modeling

When CO_2 was injected into subsurface formations, specific temperature (31.1 °C) and pressure (73.82 bar) conditions are necessary to maintain a supercritical state (Al-Khdheeawi et al., 2017; Bachu, 2001; Sohal et al., 2021). As the injected CO_2 migrates and dissolves in the saline aquifer, its mobility decreases over time, resulting in changes in CO_2 saturation within the reservoir. In our process, to simulate CO_2 saturations, we utilized Eclipse 300, a reservoir simulation software developed by Schlumberger. Our reservoir model assumes that CO_2 exists in a supercritical state and is buried at depths exceeding 800 m. For the simulation, we assigned gas diffusion coefficients of 0.001 to the CO_2 components and implemented a bottom-hole pressure (BHP) limit of 400 bars. Additionally, due to the extensive horizontal reach of our model, we assumed the presence of a non-permeable boundary. In our simulation, we only monitored the CO_2 for a limited amount of time within 100 years. Therefore, this simulation did not account for geochemical reaction between CO_2 and the mineral, which requires for a significant time span.

To perform sensitivity analysis, we focused on four key parameters: permeability, porosity, formation pressure, and temperature. In reality, the variation of the permeability has an order of magnitude larger than the other three parameters. Therefore, to accurately represent the full range of permeability values, we chose to work with the logarithm of permeability. We first selected a reference set based on a field example. Subsequently, we proceeded to individually perturb each parameter to observe and understand the impact of their changes on CO_2 saturation. To quantify the change in CO_2 saturation, we monitored the target area surrounding the injected well and tracked the variations in saturation within it. Specifically, for the purpose of quantifying the variations, we proposed a formula to compute the average saturation, as follows:

$$\overline{SG} = \frac{\sum_{i=1}^{n} Sg_i(Sg_i \geq t)}{n_{(Sg_i \geq t)}}, \tag{1}$$

where $\overline{SG}$ is the average CO_2 saturation for the entire region; Sg_i represents the saturation of CO_2 in the i grid; n represents the number of grids; t is a constant.

2.1.1. Homogeneous model

This study utilizes the geological characteristics of typical saline aquifers in the Pearl River Estuary (PRE), China. It integrates with a real CO_2 sequestration project to conduct dynamic simulation of carbon sequestration. In our reservoir modeling, we generated two models for simulation and analysis. The first one is a simple model with flat layers, which served as an ideal case for analysis. The second model has anticline and faults cutting through, which better represented a more realistic reservoir.

Our models are sized at 18 km (x) × 4 km (y) × 3 km (z). The grid spacing for reservoir simulation is 300 m (x) × 400 m (y) × 10 m (z). The deep saline aquifer has a depth of 1135 m and a thickness of 140 m. The mudstone has a porosity of 5% and a permeability of 0.1 mD, while the sandstone has a porosity of 28.5% and a permeability of 800 mD. The aquifer initially contains fully saturated saltwater, exhibiting an initial pressure of 110 bars and a temperature of 52.3 °C. These conditions are suitable for accommodating supercritical CO_2 in the reservoir (Sheng et al., 2023). Both models share identical injection parameters. The injection strategy begins in the year 2024, involving continuous CO_2 injection for 25 years, followed by an additional 75 years of monitoring through shut-in wells. During the simulation, the annual volume of CO_2 injected is 1 Mt, with a CO_2 injection rate of 1394520 sm^3/day. Fig. 1(a) and (b) show the simple model and the complex model with the injection points annotated, respectively. As for the complex model, a 20-m-thick layer of mudstone penetrates the sandstone reservoir. This enhances the sealing effect and notably diminishing the risk of leakage.

2.1.2. Heterogeneous model

All grid parameters in the heterogeneous model remain consistent with those in the homogeneous model throughout the design process. We used the SGSIM algorithm in the Stanford Geostatistical Modeling Software (SGeMS) (Mahyapour et al., 2022; Remy et al., 2009) to generate two three-dimensional random permeability fields with the same variogram model, as shown in Fig. 2. A nugget effect of 0.1 and a spherical variogram model, with weight 0.9, was used. The variogram model was set with correlation lengths to be $l_x = 10, l_y = 10$ and $l_z = 50$ (in terms of number of grid blocks) along the x, y, and z directions. The log-normal distributed permeability field had a mean of 6.68 ($\mu_{\ln k}$), and standard deviation of 0.7 ($\sigma_{\ln k}$). It is important to note that the mean log-permeability value of 6.68 corresponded to 800 mD, which is the same as that in the homogeneous case. Porosity and initial conditions were also consistent with those parameters in the homogeneous case.

In this paper, we simulated CO_2 reservoirs using both homogeneous and heterogeneous models. We utilized the van Genuchten-Mualem model (Mualem, 1976; van Genuchten, 1980) to derive relative permeability and capillary pressure curves for CO_2 storage, as shown in Fig. 3.

2.2. Rock physics modeling

When seismic waves propagate through the Earth's layers, the energy attenuates. In this paper, we only considered the intrinsic attenuation, which results from energy loss. The quality factor Q_p of the P-wave is used to quantify the intrinsic attenuation. The intensity of intrinsic attenuation is described by the frictional energy loss per cycle, as follows:

$$\frac{1}{Q_p} = -\frac{\Delta E}{2\pi E} \tag{2}$$

where E is the total energy, ΔE is the energy loss per cycle, and Q_p is the intrinsic quality factor.

The Kramers-Kronig relation establishes the relationship

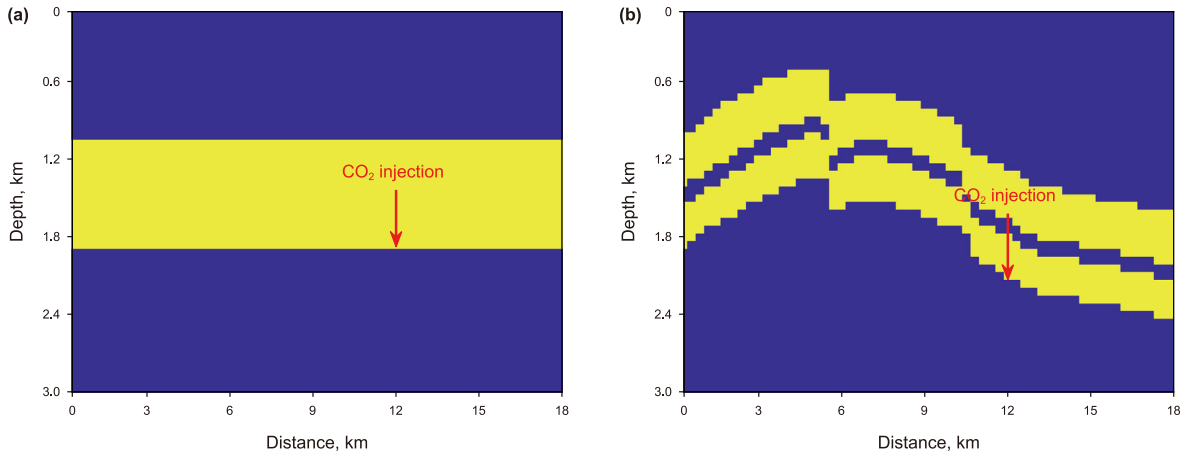

Fig. 1. 2D geological model. **(a)** A simple model with flat layers; **(b)** a more realistic model with anticline and faults cutting through.

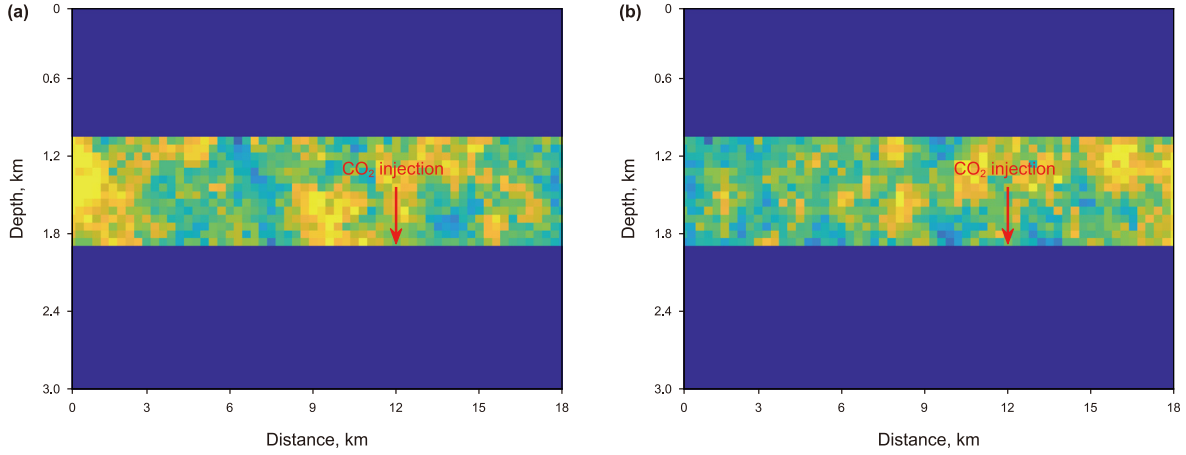

Fig. 2. Comparison of two heterogenous permeability models, **(a)** the case 1 model and **(b)** case 2 model.

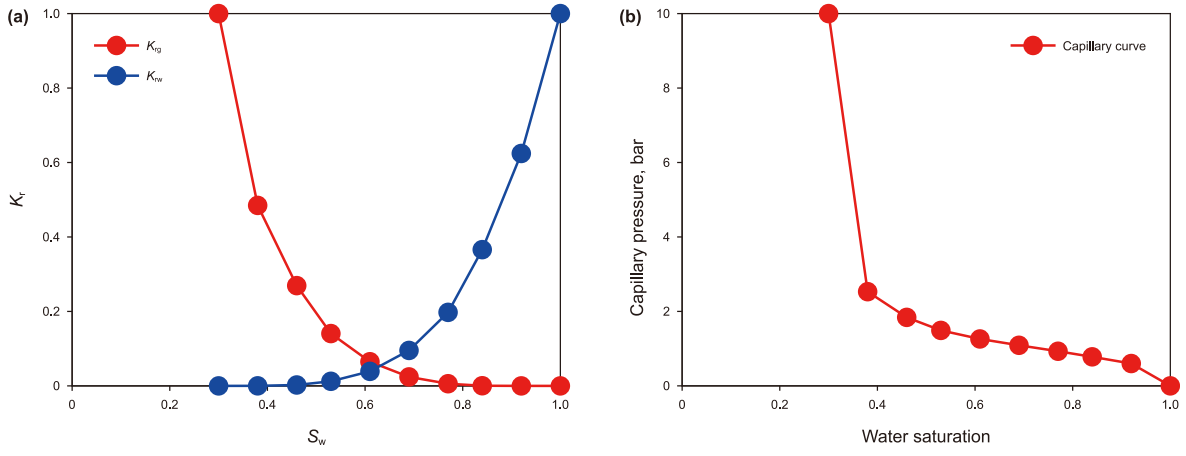

Fig. 3. **(a)** Relative permeability curve of gas-water system; **(b)** capillary curve.

between Q_p and the modulus-frequency dispersion (Kramers, 1940). We used the maximum inverse quality factor of the P-wave to compute Q_p and used the low-frequency compression modulus M_0 and the volume density ρ to calculate the P-wave velocity V_p of the rock (Shen et al., 2018c):

$$Q_{p_{max}}^{-1} = \frac{M_\infty - M_0}{2\sqrt{M_\infty M_0}}, \tag{3}$$

where M_0 represents the compression modulus at an extremely low frequency, while M_∞ corresponds to the compression modulus

at an extremely high frequency. At the low frequency, the loading is slow. This causes the oscillations of the pore pressure within a fully water-saturated patch and the patch containing both water and CO_2 to reach equilibrium. To compute the low-frequency modulus, we used the fluid substitution with V_p-only approximation (Mavko et al., 1995), as follows:

$$M_0 = M_S \frac{\phi M_{Dry} - (1-\phi)K_f M_{Dry}/M_S + K_f}{(1-\phi)K_f + \phi M_S - K_f M_{Dry}/M_S}, \quad (4)$$

where M_S is the compression modulus of mineral matrix and M_{Dry} is the compression modulus of rock skeleton. ϕ is the total porosity. K_f is the effective bulk modulus of the fluid in a rock, calculated from the harmonic average of water and CO_2.

On the contrary, at high frequencies, we used the patch saturation equation developed by Mavko et al. (2009), because the water saturated patch and the CO_2 patches are not equilibrated. So, the high-frequency compressional modulus is the harmonic average of the compressional modulus of wet rock M_W and CO_2-only rock M_G:

$$\frac{1}{M_\infty} = \frac{S_W}{M_W} + \frac{1-S_W}{M_G}, \quad (5)$$

where

$$M_W = M_S \frac{\phi M_{Dry} - (1-\phi)K_W M_{Dry}/M_S + K_W}{(1-\phi)K_W + \phi M_S - K_W M_{Dry}/M_S}, \quad (6)$$

$$M_G = M_S \frac{\phi M_{Dry} - (1-\phi)K_g M_{Dry}/M_S + K_g}{(1-\phi)K_g + \phi M_S - K_g M_{Dry}/M_S}, \quad (7)$$

where K_W and K_g are the bulk modulus of water and CO_2, respectively, and S_W is the water saturation.

To compute the P-wave velocity V_p of the rock, we used the low-frequency compression modulus M_0 and the volume density ρ, as shown below:

$$V_p = \sqrt{\frac{M_0}{\rho}}. \quad (8)$$

2.3. Seismic modeling

It is well known that seismic wave propagates in media filled with gas (e.g., CO_2) will exhibit amplitude dissipation and phase dispersion. To accurately describe the wave propagation properties in attenuating media, a series of attenuation theories have been developed over the years (Carcione et al., 1988). One of widely used theory is the constant Q (CQ) attenuation theory (Carcione et al., 2002; Shen et al., 2018a, 2018b), proposed by (Kjartansson, 1979). Building on the CQ theory, many viscoacoustic wave equations have been derived to simulate the characteristics of seismic wave propagation. In this study, we employed the fractional Laplacian viscoacoustic wave equation proposed by Zhu and Harris (2014) to perform forward modeling, which can be expressed as

$$\frac{1}{c^2}\frac{\partial^2 p}{\partial t^2} = \eta\left(-\nabla^2\right)^{\gamma+1} p + \tau\frac{\partial}{\partial t}\left(-\nabla^2\right)^{\gamma+1/2} p, \quad (9)$$

where $c = v_0\cos(\pi\gamma/2)$, v_0 is the P-wave velocity, $\gamma = \arctan(1/Q_p)/\pi$ is a dimensionless variable, Q_p is the quality factor that characterizes the strength of attenuation. The coefficients η and τ are $\eta = -v_0^{2\gamma}\omega_0^{-2\gamma}\cos(\pi\gamma), \tau = -v_0^{2\gamma-1}\omega_0^{-2\gamma}\sin(\pi\gamma)$.

In Eq. (9), when $Q_p \to \infty$, Eq. (9) becomes the acoustic wave equation.

2.4. Work flow

Fig. 4 shows the steps of the research: First, we input the geological model into the reservoir simulator to compute the post-injection CO_2 saturation. Then we computed Q_p in Eq. (3) and V_p in Eq. (8). Based on these elastic models, we were able to generate the time-lapse seismic datasets using Eq. (9). To perform the analysis of the seismic response to CO_2 saturation, we performed reverse-time migration to image the subsurface which better display the distribution of the CO_2 plume.

3. Results and discussion

3.1. Reservoir simulation results

3.1.1. Homogeneous model

Fig. 5(a) and (b) illustrate the distribution of the migration of supercritical CO_2 following injection into a single-well, along with the plume simulation. It shows the variation in CO_2 saturation over 25-years period of injection and monitoring for 100 years. It is evident that with the continuous injection of CO_2, the CO_2 plume eventually accumulated at the top, forming a "funnel-shaped" structure, and regions with higher concentration gradually moved upward over time. Despite the expansion of the plume, it is clear that the concentration decreased, attributed to the CO_2 dissolving into the reservoir water over time.

From Fig. 5(a) and (b), it is observed that near the injection well, as CO_2 continues to be injected, the formation water in the reservoir is continuously displaced. After 25 years, the free CO_2 exhibits a horizontal migration distance of 4200 m, with an average annual speed of 168 m. After 100 years, the plume covers a maximum horizontal migration distance to 5100 m, with an average annual speed of 51 m. While the increase in horizontal migration distance was not substantial, the plume suggests a larger and farther range of overall migration. Considering only the average annual speed, it is evident that during the injection period, the CO_2 migration speed was relatively rapid. However, after the injection stopped, the CO_2 in the reservoir gradually diminished. At the same time, it becomes evident that with the change of time, CO_2 saturation gradually migrated to the cap layer without any signs of leakage. This shows the cap layer's effective sealing properties. In Fig. 5(c), the plume approaches and barely touches the fault at the 25 year. By the 100 years (Fig. 5(d)), the CO_2 saturation continued to move forward and upward, resulting in a horizontal distance approximately 1200 m further away from the fault.

3.1.2. Heterogeneous model

Fig. 6 illustrates the distribution of CO_2 migration in the reservoir over a 100-year period in the heterogeneous model. From the simulation results, we observe that the range of CO_2 saturation gradually increased over time, which is consistent with the conclusions drawn from the homogeneous model. However, comparing Fig. 5(a) and (b) with Fig. 6, it is evident that the range of the CO_2 plume in the heterogeneous model is larger than that in the homogeneous model. This is due to the stochastic distribution of permeability near the injection well in the heterogeneous model and exceeds that of the homogeneous model. In addition, areas with higher permeability enables easier migration and storage of CO_2, thereby resulting in an increased size of CO_2 plume. In Fig. 6(a)

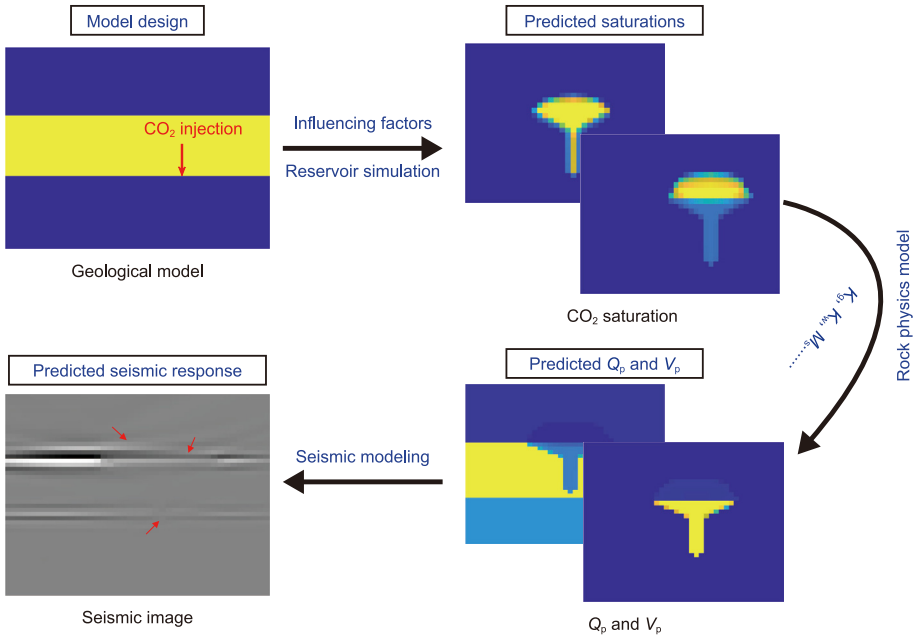

Fig. 4. Flow chart for predicting the sensitivity of geological environmental factors to Q_p, V_p, and seismic response in CO_2 reservoir simulation.

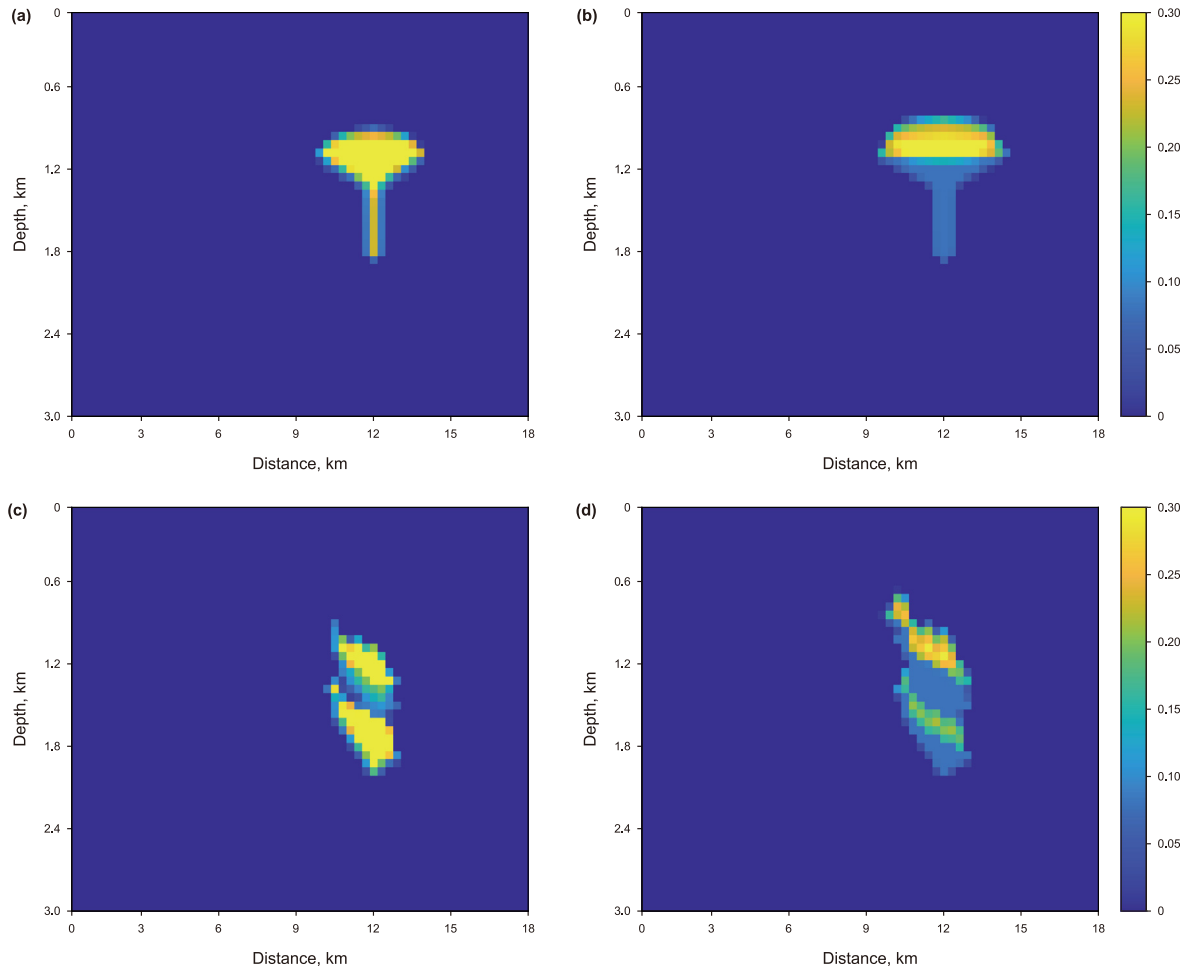

Fig. 5. **(a)** CO_2 injection for 25 years and **(b)** 100 years in a simple model; **(c)** CO_2 injection for 25 years and **(d)** 100 years in a complex model.

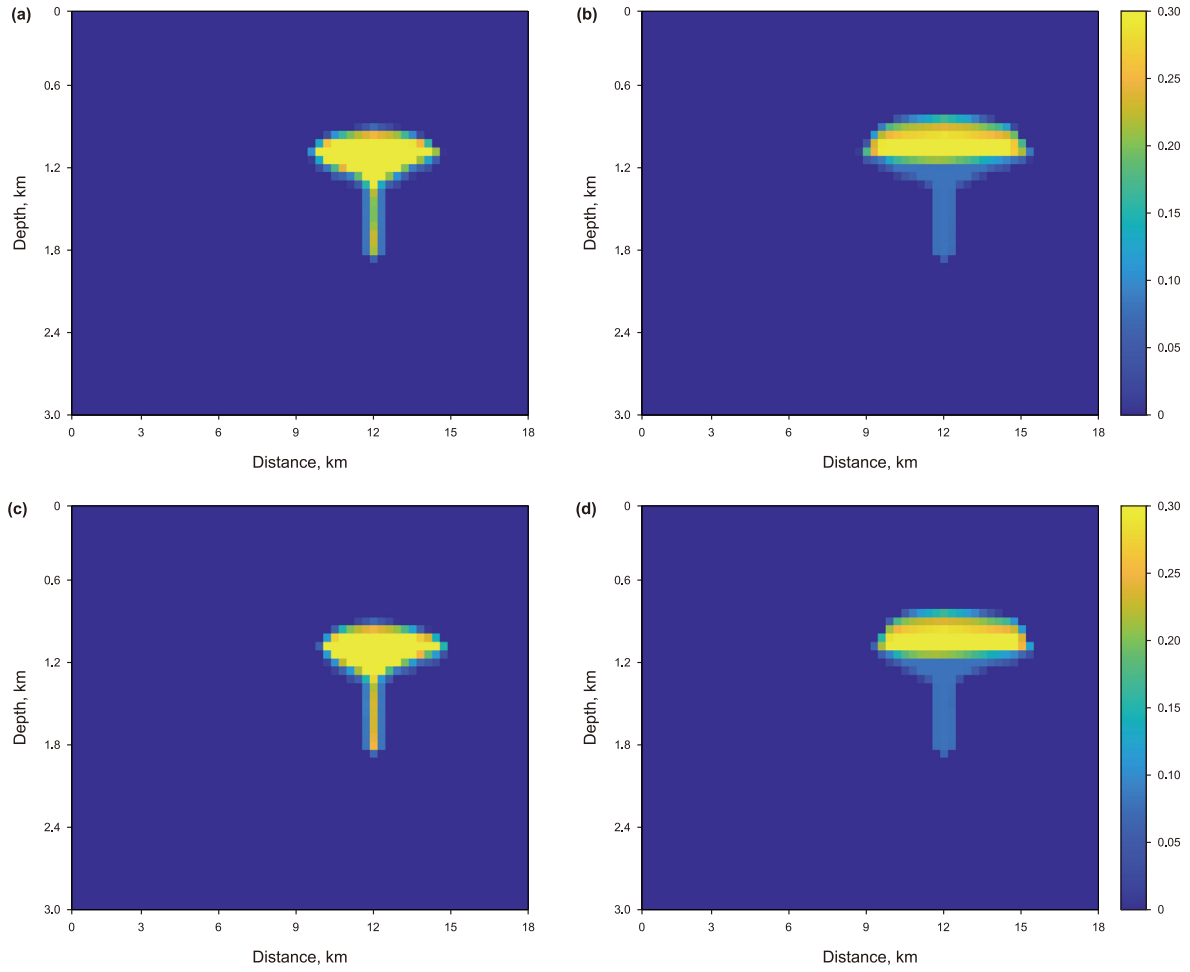

Fig. 6. **(a)** CO_2 plume distribution over 25 years and **(b)** 100 years in heterogeneous case 1 model; **(c)** CO_2 injection over 25 years and **(d)** 100 years in heterogeneous case 2 model.

and (b), the CO_2 plume extends further than that in Fig. 6(c) and (d). This is mainly due to the higher permeability in the case 1 model compared to the case 2 model. Furthermore, in Fig. 6(c) and (d), CO_2 migration extends notably further to the right of the injection well than to the left. This is primarily due to slightly higher permeability on the right side in the heterogeneous case 2 model (Fig. 2(b)).

3.2. Sensitivity analysis of reservoir modeling

To gain deeper insights into the impact of diverse geological environmental factors and aquifer properties on CO_2 saturation post-injection, we selected four influential parameters for single-factor sensitivity analysis. These parameters included porosity, permeability, temperature, and formation pressure. It is worth noting that the permeability variation is actually an order of magnitude larger than the other three parameters. Hence, in order to accurately depict the full range of permeability, we opted to work with the log-permeability ($\log(K_h)$), note that $\log(K_h)$ is a logarithmic function with a base number of 10. Notably, the change in the horizontal permeability (K_h) resulted in a corresponding change in the vertical permeability (K_v), given that the ratio between the two (K_h/K_v) remained constant. The specific value for this ratio can be found in Wainwright et al. (2013). This section primarily focuses on performing sensitivity analysis using the reservoir's CO_2 saturation at the 100th year.

Table 1
Selection of model parameters for sensitivity analysis.

Parameters	−30%	−20%	−10%	Base	+10%	+20%	+30%
Temperature, °C	36.61	41.84	47.07	52.3	57.53	62.76	67.99
Formation pressure, bar	77	88	99	110	121	132	143
Porosity, %	19.95	22.8	25.65	28.5	31.35	34.2	37.05
Log(K_h), mD	107	210	410	800	1561	3046	5943

The parameter settings are detailed in Table 1, which we used for dynamic carbon sequestration simulations. We utilized data from a real CO_2 sequestration project along with actual well logging data. This helps us obtain a reference parameter set of these four parameters, shown in the middle column of this table. Each time, we perturbed one parameter of our base set by a certain percentage, to examine the change of the CO_2 plume distribution.

3.2.1. Sensitivity analysis of homogeneous reservoir

3.2.1.1. Sensitivity analysis of simple models. As shown in Fig. 7(a) and (b), it is evident that elevated temperatures promoted the migration and distribution of supercritical CO_2. This phenomenon is primarily attributed to the increased kinetic energy of CO_2 molecules within the reservoir, due to the rise in temperature. Consequently, a higher temperature results in a more active gas phase CO_2 (Perera et al., 2012). With rising temperatures, CO_2 in the reservoir ceases to dissolve with water, instead persisting in a supercritical state, leading to an increase in mobile CO_2. Based on Henry's law, at a specific temperature and equilibrium state, the solubility of CO_2 in a liquid is directly proportional to the

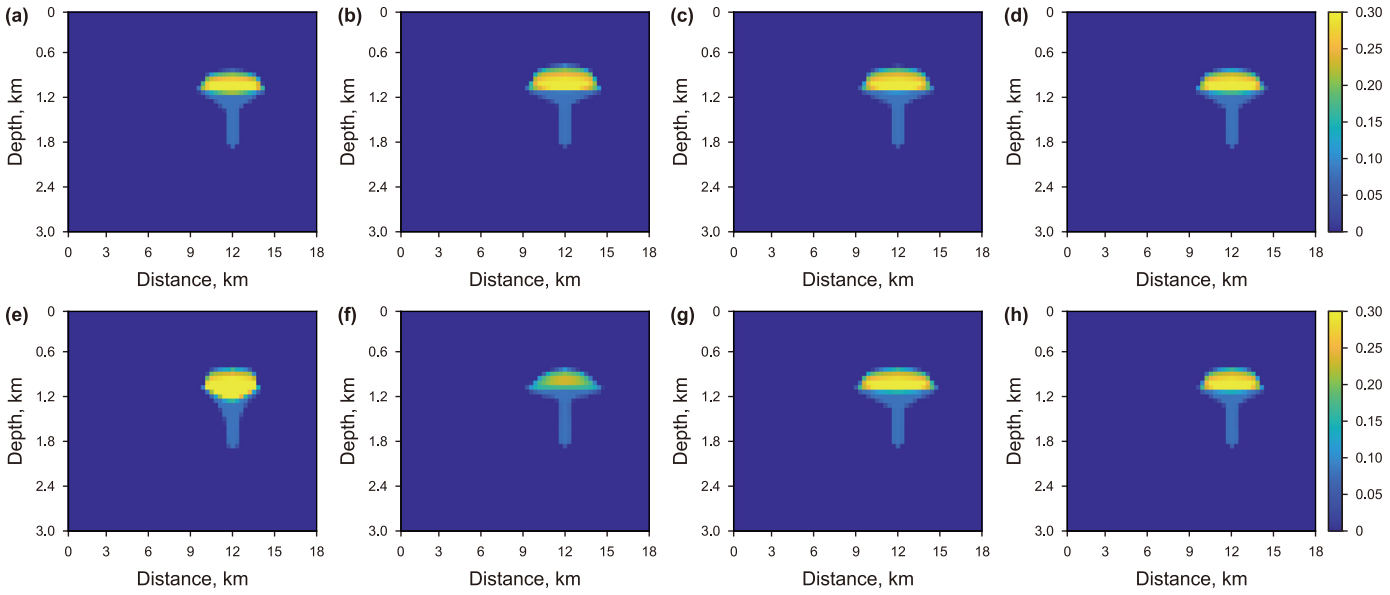

Fig. 7. Distribution of CO_2 saturation after 100 years of storage in a simple model. **(a)** Temperature: −30%; **(b)** temperature: +30%; **(c)** formation pressure: −30%; **(d)** formation pressure: +30%; **(e)** log(K_h): −30%; **(f)** log(K_h): +30%; **(g)** porosity: −30%; **(h)** porosity: +30%.

equilibrium pressure of CO_2. With increasing formation pressure, the available "space" for injecting CO_2 into the reservoir diminishes, resulting in reduced CO_2 injection capacity and subsequently lower CO_2 concentrations within the reservoir (Perera et al., 2016). Consequently, higher formation pressure leads to increased dissolved CO_2 production and reduced gas saturation. As a result, the range of the CO_2 diffusion halo gradually diminishes, as shown in Fig. 7(c) and (d).

In Fig. 7(e) and (f), the log(K_h) has a significant impact on the transport of CO_2 saturation. An increase in the log(K_h) during the simulation enhances the rock's capacity to accommodate the flow of CO_2. The increasing permeability allows the fluid to penetrate larger distances and occupy more space in the reservoir, leading to a larger contact area between CO_2 and water. As a result, an increasing amount of CO_2 dissolved in water results in a decrease in the free-phase CO_2 saturation within the reservoir. As can be seen from Fig. 7(g) and (h), the greater the porosity, the lower the CO_2 saturation in the reservoir. Greater reservoir porosity may signify increased pore space within the rock, but it may also indicate improved connectivity among the pores, which facilitates CO_2 diffusion and migration. Moreover, increased porosity in the reservoir can enhance permeability, making it easier for CO_2 to flow through the rock's pores, reducing the retention time of CO_2 in the reservoir and subsequently lowering CO_2 saturation.

To further characterize the migration of CO_2 within the grid, we measured the maximum horizonal distance of the CO_2 plume, and showed the measurement of each parameter set in Fig. 8(a). Fig. 8(a) illustrates that the migration distance increases with higher permeability and temperature, while decreases with porosity and formation pressure. Specifically, the variation in the log of permeability results in the most significant change in the CO_2 migration distance, from 4200 m to 5700 m. Conversely, increasing porosity confines the horizontal migration of CO_2 the most, reducing the distance from 6000 m to 4800 m. Because larger pores retaining a significant portion of the CO_2 and hindering its movement to adjacent pores. While compared with the permeability and porosity, the other two parameters of formation pressure and temperature has less influences on the CO_2 migration.

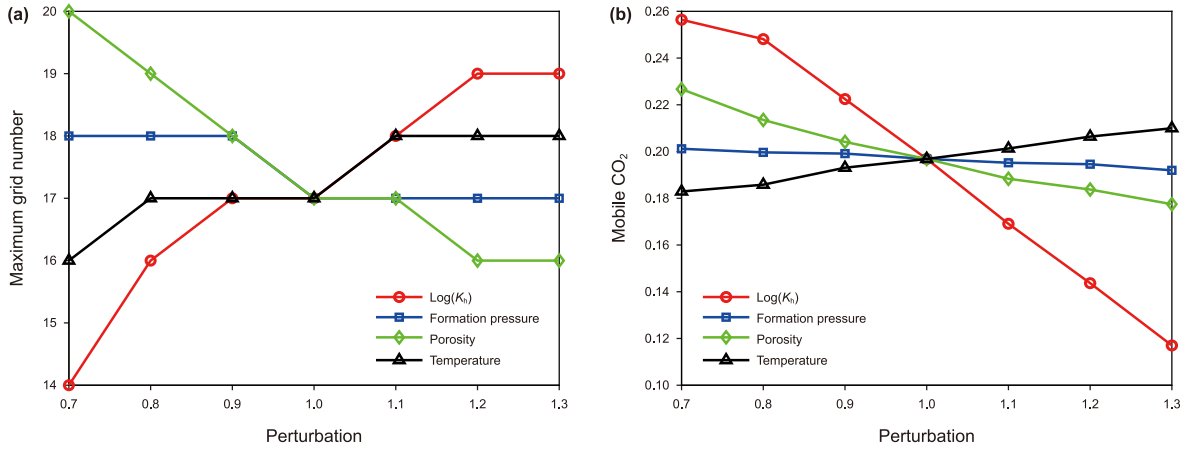

Fig. 8. **(a)** The evolution of the maximum grid count for the transverse transport of CO_2 across the entire region over 100 years in a simple model; **(b)** the key parameter 100 years $Sg_i \geq 0.08$ CO_2 saturation of sensitivity analysis.

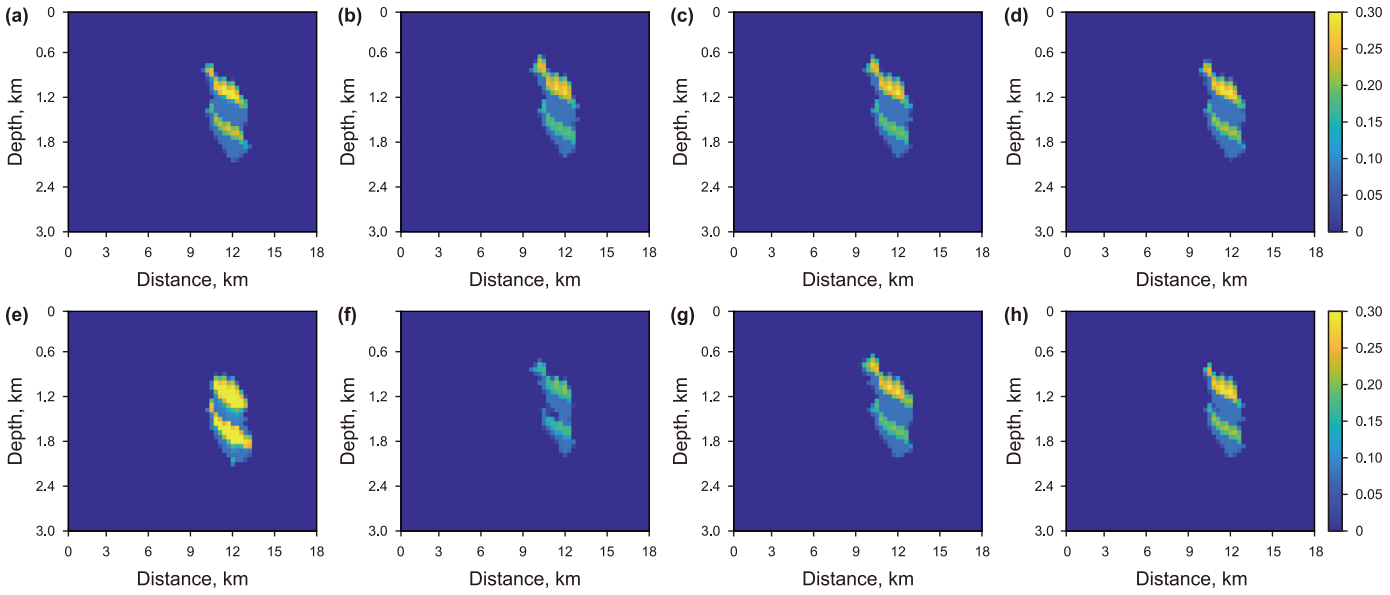

Fig. 9. Distribution of CO_2 saturation after 100 years of storage in a complex model. **(a)** Temperature: −30%; **(b)** temperature: +30%; **(c)** formation pressure: −30%; **(d)** formation pressure: +30%; **(e)** log(K_h): −30%; **(f)** log(K_h): +30%; **(g)** porosity: −30%; **(h)** porosity: +30%.

To examine the sensitivity of these parameters to CO_2 saturation, we used Eq. (1) to compute the average saturation by setting the threshold parameter t to 0.08. Fig. 8(b) shows the sensitivity analysis of CO_2 saturation, indicating that permeability is the most contributing factor to the CO_2 saturation change. According to Darcy's law, permeability is linked to the flow velocity through the porous medium. Therefore, an increase in permeability raises the rate of CO_2 passage under a consistent pressure gradient, leading to a larger contact area with water. This results in the production of more dissolved CO_2 and decreased CO_2 saturation with higher permeability. In addition, we can observe from Fig. 8(b) that the CO_2 saturation decreases with the porosity, same observation as in Fig. 7(g) and (h) with the same explanation.

3.2.1.2. Sensitivity analysis of complex models. We performed the same sensitivity analysis of the CO_2 saturation and CO_2 migration distance for the complex models. As shown in Fig. 9, the simulation results for each perturb parameter. Fig. 10(a) and (b) show the variations of the CO_2 migration distance and average saturation with the changes in parameters, respectively. We could draw the same conclusions as the simple model.

Furthermore, the complex model has fault cutting across the target reservoir. As for the test in this model, we studied the effects of faults on the transport and distribution of CO_2. As shown in Figs. 7 and 9, the CO_2 plume migrated further in the lateral distance, when the temperature and log(K_h) increases, while formation pressure and porosity decrease. Therefore, temperature and log(K_h) help the CO_2 plume reach the fault at an earlier time, and the formation pressure and porosity prevent the CO_2 plume from moving towards the faults.

To further investigate how these various influencing factors impact the plume migration across the fault, we performed a quantitively sensitivity analysis, as shown in Fig. 11. To compute Fig. 11, we first selected the midpoint located at $x = 10500$ m, which is on the left side of the fault. Then we found that the maximum value of the saturation over the depth for this particular midpoint. This maximum value changed with time, thus we plot this value over time in Fig. 11. We can observe that the saturation values for this selected point increases at the beginning and slightly drop down since the injection stops.

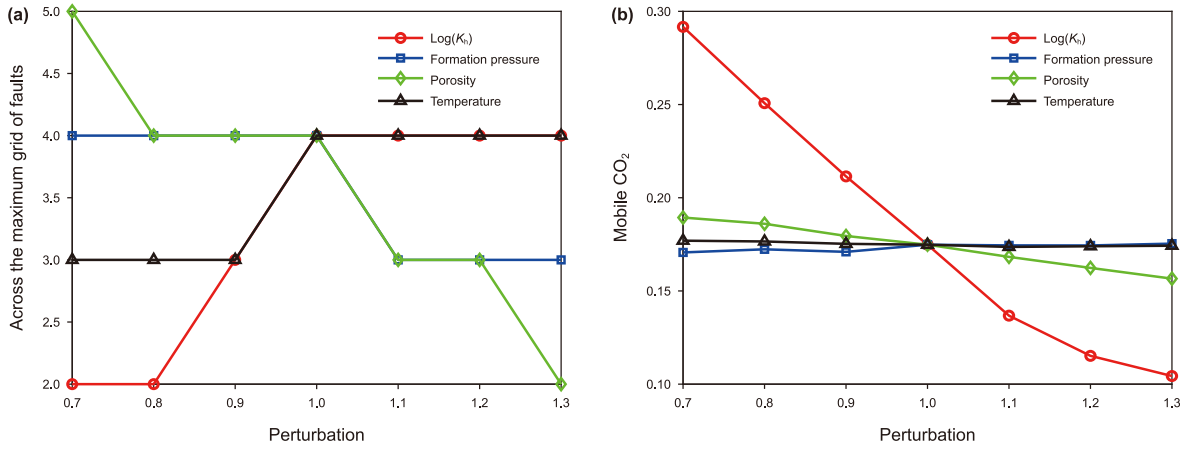

Fig. 10. **(a)** CO_2 saturation illustrates the maximum number of horizontal grids across the fault; **(b)** regional CO_2 saturation of $Sg_i \geq 0.08$ over 100 years in complex models.

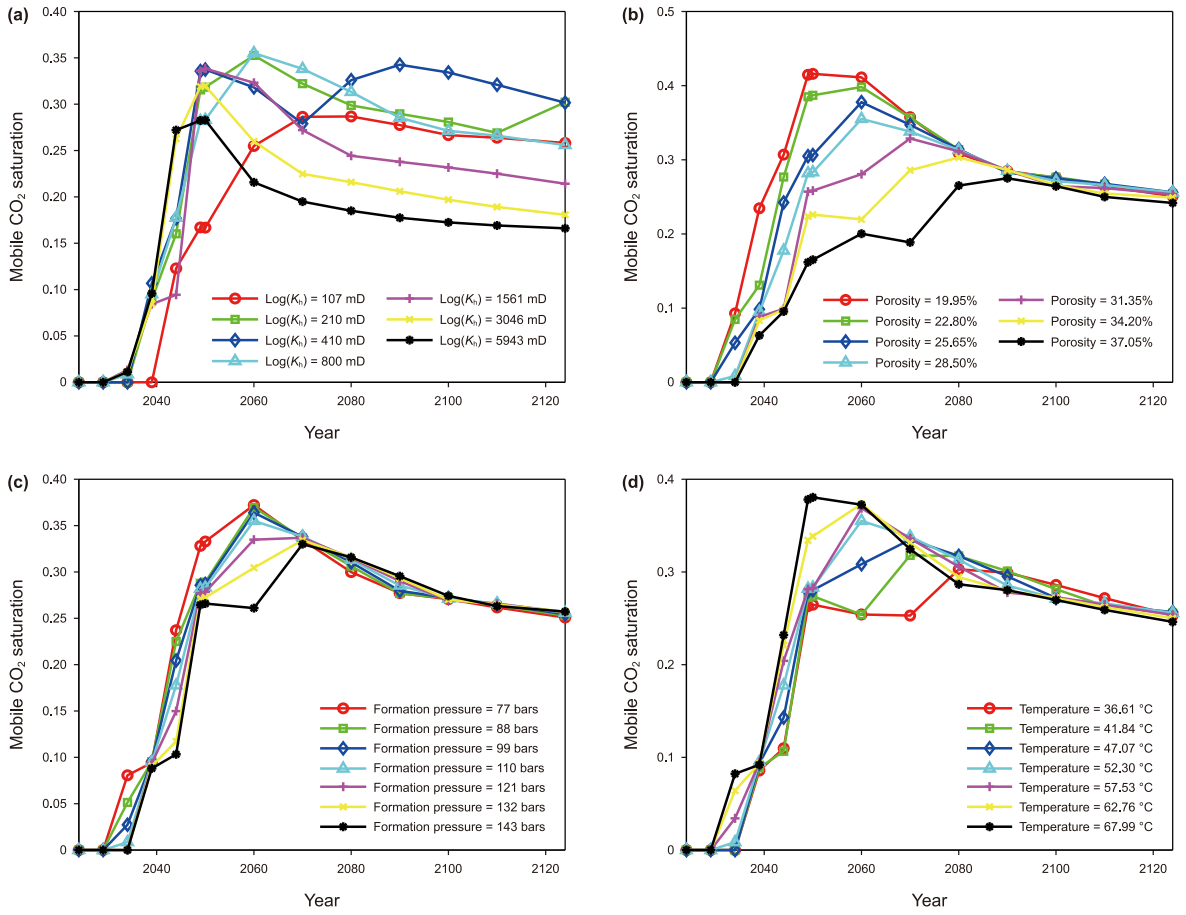

Fig. 11. Temporal dynamics of CO_2 saturation migration to fault: a 100-year perturbation study on **(a)** log(K_h), **(b)** porosity, **(c)** formation pressure, and **(d)** temperature.

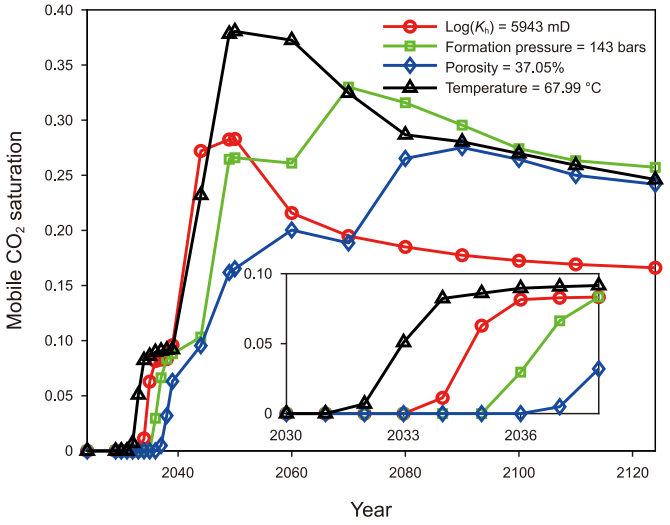

Fig. 12. Distribution of the maximum simulated mobile CO_2 saturation over 100 years to the fault over time.

In addition, in Fig. 11, the curves initially start at zero during the CO_2 injection, because the plume hasn't reached to this point yet. Their onset time, at which the curve becomes non-zero, means when the plume has crossed the fault and came to this point. Therefore, the onset point of these curves can effectively reflect how fast the plume has moved across the fault. The increasing log(K_h) and temperature, moved the plume migrate faster and migrate over the faults more quickly. While porosity and formation pressure slow down the migration speed, the fault-crossing time became later. Among all the curves, we selected the ones corresponding to the maximum parameters, including log(K_h), porosity, formation pressure, and temperature increased by 30%, and plot their correspondent curve in Fig. 12. We can observe that high temperature makes the curve with the steepest slope and shortest onset time (as see the zoom-in box), indicating that CO_2 migrated to this area at the earliest. This phenomenon can be attributed to higher temperatures enhancing the activity of CO_2 and resulting in a greater amount of free CO_2 within the reservoir.

3.2.2. *Sensitivity analysis of heterogeneous reservoir*

We conducted a similar sensitivity analysis on the CO_2 saturation and migration distance in the heterogeneous model. We reach the same conclusions as the homogeneous model. Increasing temperature and log(K_h) result in the lateral migration distance of the CO_2 plume expanding further. Meanwhile, increasing formation pressure and porosity lead to a decrease in CO_2 saturation in the reservoir. To compare the sensitivity of the four key parameters in heterogeneous models, we perturbed these parameters using the same method as the homogeneous model. We focused on permeability, porosity, formation pressure, and temperature. Utilizing Eq. (1), we conducted single-factor sensitivity analysis on CO_2 saturation across the entire region. The result indicates that the findings in the heterogeneous models align with those in the homogeneous model. Permeability is the most sensitive parameter to CO_2 saturation, as shown in Fig. 13.

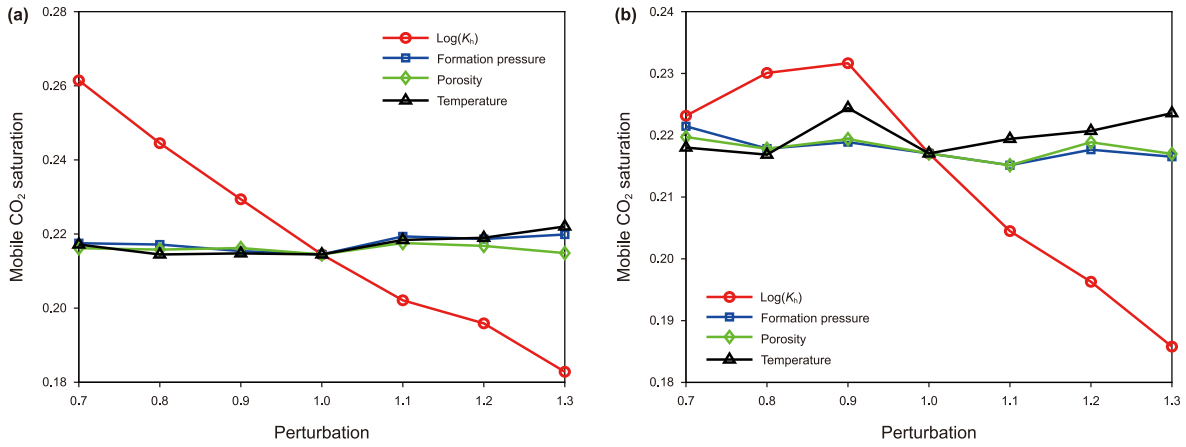

Fig. 13. The CO_2 saturation in regions where $Sg_i \geq 0.08$ over 100 years in heterogeneous models **(a)** with case 1 model and **(b)** with case 2 model.

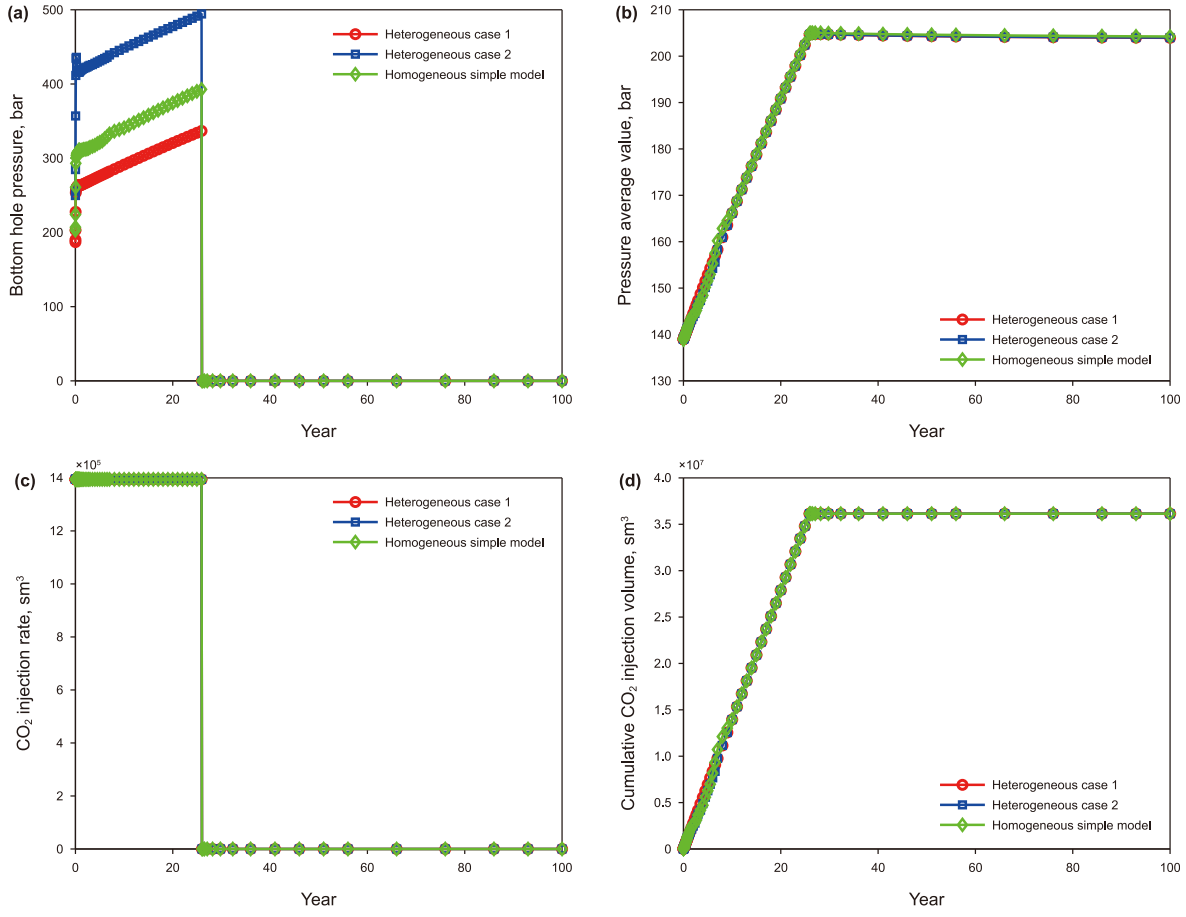

Fig. 14. **(a)** The curve of bottom-hole pressure variation over time after 100 years of CO_2 injection in homogeneous and heterogeneous models; **(b)** the trend of average reservoir pressure over time; **(c)** the curve depicting the variation of CO_2 injection rate over time; **(d)** the plot showing the variation of cumulative CO_2 injection volume over time.

During CO_2 sequestration simulation, evaluating post-injection sealing is crucial for long-term stable storage. We analysed post-injection effects in both homogeneous and heterogeneous models. This analysis focuses on variations in bottom-hole pressure, average reservoir pressure, CO_2 injection rate, and cumulative CO_2 injection volume, as shown in Fig. 14. Fig. 14(a) illustrates that during the CO_2 injection period (25 years), pressure gradually increases within the reservoir, leading to an increase in bottom-hole pressure. After injection stopped, reservoir pressure gradually decreases, leading to a reduction in bottom-hole pressure. One primary concern is the relatively small size of the model 18 km (x) × 4 km (y) × 3 km (z), which may contribute to rapid pressure build-up during injection.

Furthermore, during the CO_2 injection, the maximum bottom-hole pressure of the blue line in Fig. 14(a) for case 2 model exceeds the specified 400-bar bottom-hole pressure boundary condition. Because of the relatively lower average permeability of the grid cells through which the CO_2 plume migrated, the rate of CO_2

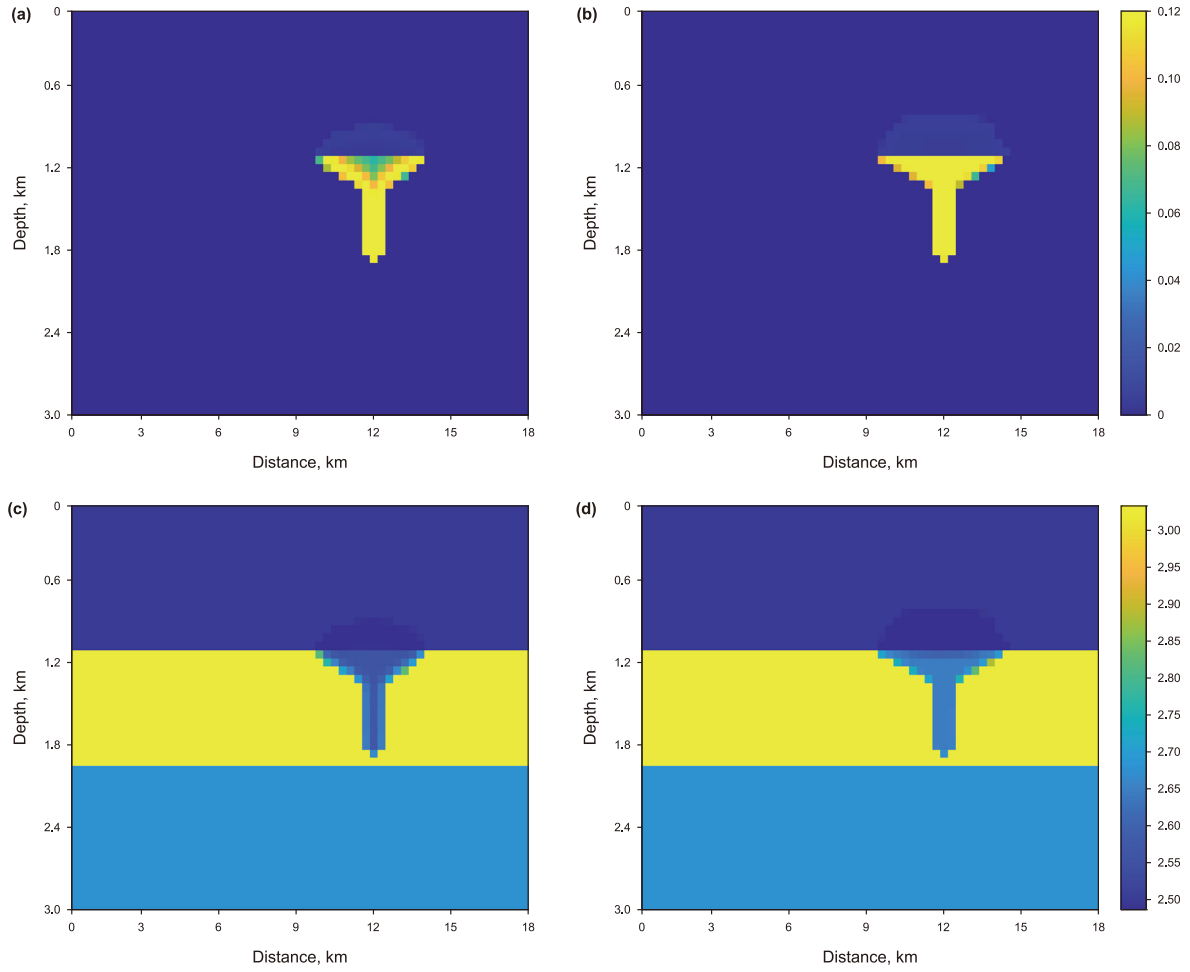

Fig. 15. **(a)** 25-year $1/Q_p$ of CO_2 injection in a simple model; **(b)** monitoring reservoir $1/Q_p$ for 100 years after CO_2 injection; **(c)** CO_2 injection for 25 years and **(d)** 100 years V_p.

migration is slower. To inject an equivalent amount of CO_2 within the same timeframe and maintain a sufficient injection rate, we needed to apply greater bottom-hole pressure. This helps overcome the resistance of the rock medium. However, in the heterogeneous case 1 model, the bottom-hole pressure is lower than that of the homogeneous model. This suggests that the average permeability around the injection well in the grid cells is higher than that of the homogeneous model. After injection stopped, the bottom-hole pressure gradually decreases in both homogeneous and heterogeneous models. From Fig. 14, we observe that in both homogeneous and heterogeneous models, the difference in bottom-hole pressure during CO_2 injection is notable. However, the impact on average pressure in other reservoirs, CO_2 injection rate, and cumulative CO_2 quantity appears insignificant in this dynamic CO_2 plume trapping process, as shown in Fig. 14(b)–(d).

In summary, this study analyses the results of dynamic reservoir simulations of CO_2 plumes. It also conducts sensitivity analyses on the four key parameters of homogeneous and heterogeneous models. We found consistent results between homogeneous and heterogeneous models. Permeability is the most sensitive parameter to CO_2 saturation, as shown in Figs. 8(b), 10(b) and 13. These findings suggest that the sensitivity analysis of CO_2 saturation has minimal impact in this study's sealing simulation. It applies to both homogeneous and heterogeneous models. Therefore, in the next section, we will conduct sensitivity analysis on Q_p and V_p using an ideal homogeneous flat simple model.

3.3. Rock physics modeling

In this section, we computed V_p and Q_p using Eqs. (2)–(8). Fig. 16(a) and (b) show the V_p and Q_p values with respect to CO_2 saturation. Both figures show a critical point at which Q_p and V_p reaches to their minimal value with saturation. Thus, attenuation first increases with CO_2 saturation, and increases after the critical point. However, the velocity decreases when the CO_2 starts to inject, because CO_2 reduces the rock modulus. Meanwhile, CO_2 reduces the density of the fluid, so after a critical point, the influence of the density change dominates and the velocity builds up again.

Same as above, we perturbed four parameters: permeability, porosity, formation pressure, temperature, and explored which parameter most influenced V_p and Q_p. In the following section, we only showed the results and conclusions homogeneous flat simple model, because both the homogeneous and the heterogeneous models yield identical observations. As for the simple model, we established the baseline velocity values as $V_p = 2500$ m/s for the first layer, $V_p = 3033$ m/s for the second layer, and $V_p = 2680$ m/s for the third layer. In terms of Q_p, the baseline value is set at 100,000, which means no attenuation within the seismic frequency range before CO_2 injection.

Fig. 15(a) and (b) illustrate the $1/Q_p$ (attenuation) model at the 25-year and 100-year, respectively. Fig. 15(c) and (d) show the velocity model at the 25-year and 100-year, respectively. In cases

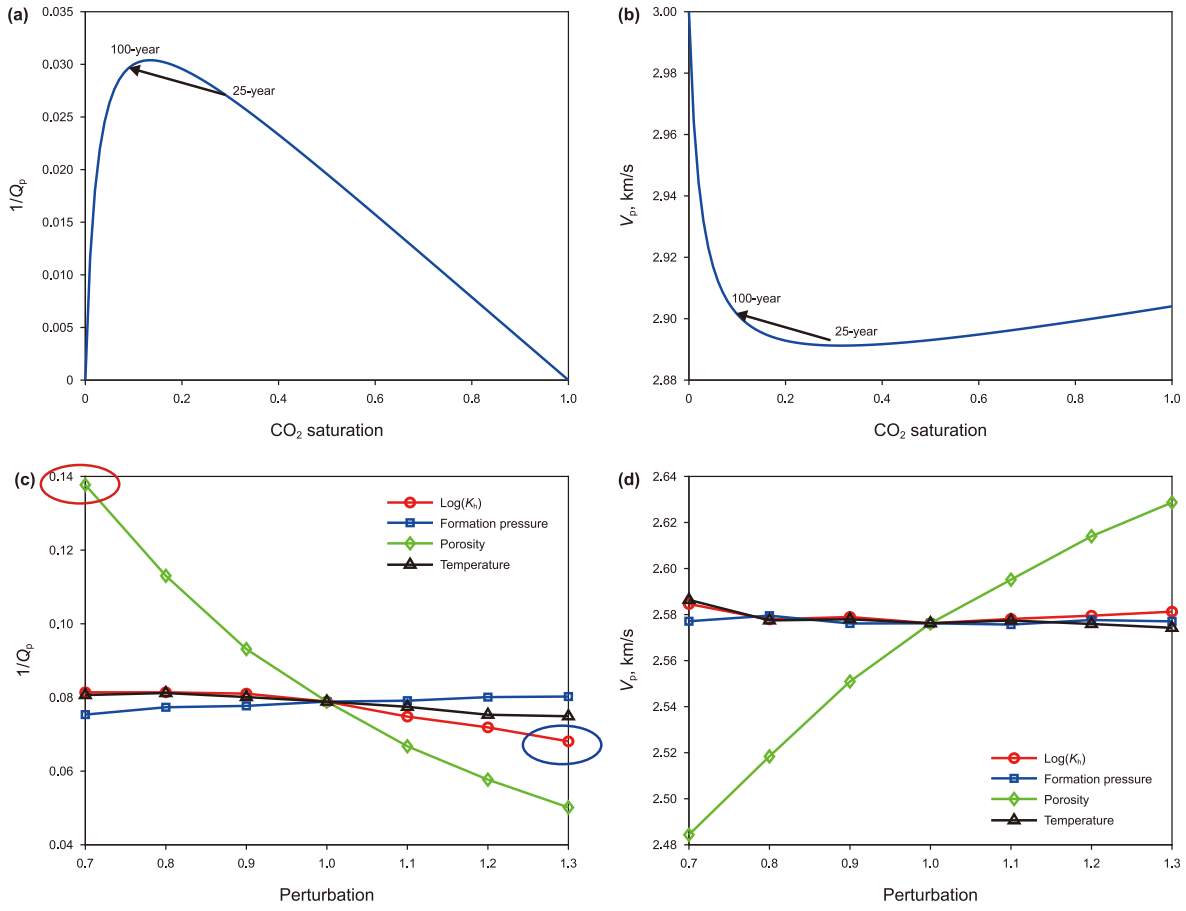

Fig. 16. The relationship between CO_2 saturation **(a)** $^1/_{Q_p}$ and **(b)** V_p; the sensitivity of **(c)** $^1/_{Q_p}$ and **(d)** V_p in the influencing factor.

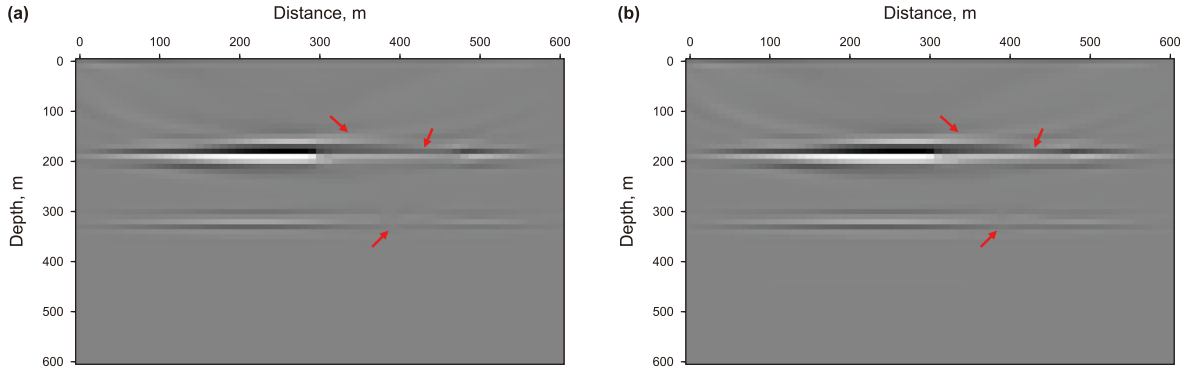

Fig. 17. Time-lapse migration imaging results of **(a)** the sensitive model and **(b)** the insensitive model following the injection of CO_2.

where porosity remains constant, a gradual increase in CO_2 saturation within the reservoir from 25 to 100 years, consequently leading to an increase in attenuation. Notably, the rate at 25 years is distinctly lower than the rate observed at 100 years (see Fig. 15(c) and (d)). We notice the attenuation increases from the baseline to the year of 25, and continues to increase at the year of 100. This is because the saturation range of our simulated plume is from 0.1 to 0.3, and the attenuation keeps increasing as indicated by the arrow in Fig. 16(a). On the other hand, the velocity decreases at the year of 25 and increases afterward. As indicated by the arrow in Fig. 16(b), we see the from year of 25 to year of 100, saturation decreases and moves across the critical point. So, we see the velocity increased at year of 100 as shown in Fig. 15(d) when compared with the year of 25.

Fig. 16(c) and (d) show the sensitive analysis of the four influential parameters to V_p and Q_p at the year of 100. Although the permeability has the most substantial impact on CO_2 saturation, Fig. 16 shows that porosity has the most significant impact on both V_p and Q_p. Because the porosity changes the portion of the movable CO_2, influencing the modulus and density of the rock and altering the cross-flow in the pores. Additionally, Fig. 16 indicates that increased porosity reduces attenuation and enhances velocity, in contrast to natural gas behaviour (Mavko et al., 1995; Shen et al., 2018c). Due to the short-term migration of the CO_2 compared

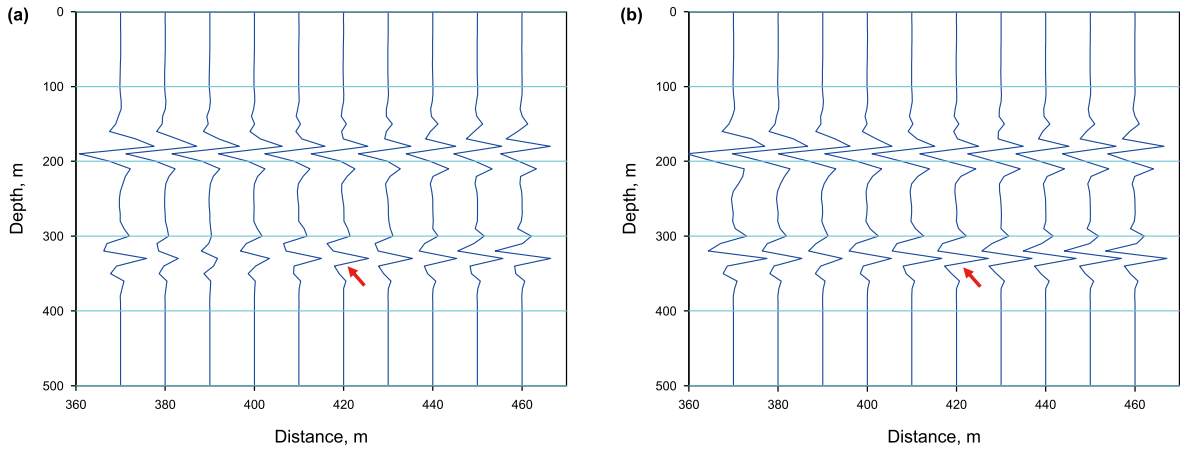

Fig. 18. Seismic tracing after CO_2 injection in the **(a)** sensitive model and **(b)** insensitive model.

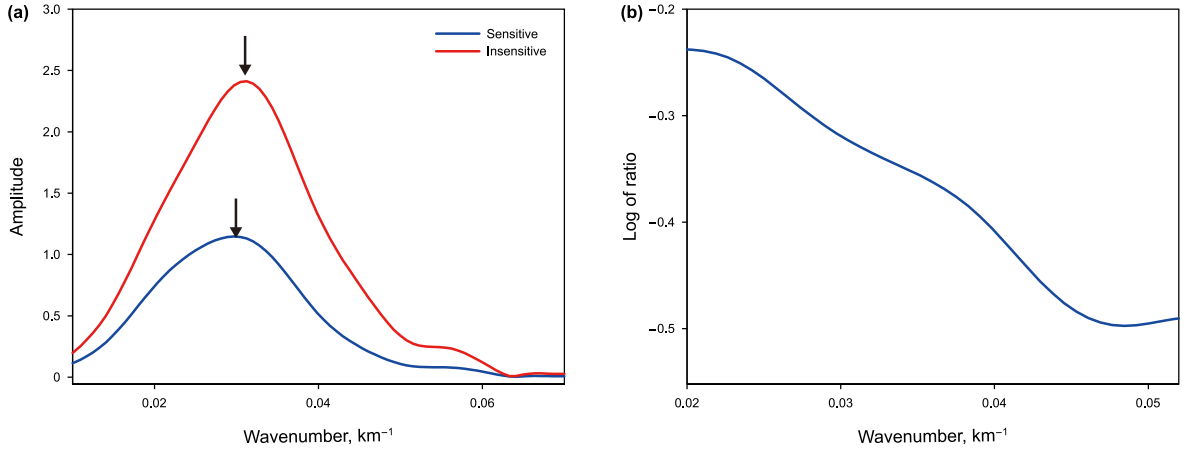

Fig. 19. **(a)** The spectra of Fig. 17(a) (blue) and Fig. 17(b) (red); **(b)** the logarithm of the ratio of the blue curve to the red curve in Fig. 17(a), note that log(·) is a logarithmic function with a base number of e.

with natural gas and the limited amount of the injection volume. The large porosity decreases the CO_2 saturation, causing the saturation become smaller than the critical point at 100 years, so that to reduce the attenuation and enhance the velocity before critical point, as shown in Fig. 16.

3.4. Seismic image

Based on the above analysis, using visco-acoustic wave Eq. (9), we performed seismic forward modeling and reverse time migration without compensation, where with the time-lapse models being the greatest and least sensitive to Q_p and V_p, respectively. Specifically, the most sensitive parameters to Q_p and V_p is porosity as we described above, and the permeability is the relatively least sensitive. We chose the sensitive model as denoted by red circle in Fig. 16(c), and the insensitive model as denoted by blue circle in Fig. 16(c). The forward modeling of the time-lapse data considers both velocity changes and attenuation changes over time, while the migration only accounts for the velocity change without compensating for any attenuation. Therefore, Fig. 17 primarily emphasizes the attenuation effects. In comparison to Fig. 17(b) and 17(a) generated by the sensitive model has stronger seismic response with stronger attenuation, in terms of the weakened amplitudes, decreased resolution and distorted phase.

To better display the attenuation effects, we selected 10 seismic traces and showed their zoom-in plots in Fig. 18. The zoom-in locations are situated near the CO_2 injection well. We noticed that the amplitudes in Fig. 18(a) is notably weaker than the one in Fig. 18 (b). In this synthetic example, we expected the wavelet of our migrated events being the zero phase. Attenuation disperse the phase velocity and distort the wavelets. We could see that the sensitive model attenuated the events further and distorted the wavelet further away from the zero phase.

To better evaluate the attenuation effect, we computed the spectra of the area around the CO_2 injection well, as shown in Fig. 19(a). We defined the red curve in Fig. 19(a) as insensitive spectra, which means the spectra is computed from the image migrated using the insensitive model. Same for the blue curve in Fig. 19(a), we defined it as the sensitive spectra. We saw that the sensitive spectra have a large attenuation effect, which has a larger amplitude decays especially at the high frequencies. Therefore, the central frequencies of the blue curve have a downward shift to the lower frequencies, as the arrow indicated. To quantify the spectral decay, we employed the spectral ratio method (Tonn, 1991). Based on the theory of spectral ratio method, we computed the ratio of the blue curve and red curve. Then, we took the logarithm of the ratio, resulting in a linear line over the frequencies. The value of the slope effectively quantifies the difference of the attenuation effects between the blue and red spectra. Fig. 19(b) shows a curve that could be approximated as a linear line. This line has a notable

negative slope, indicating the blue curve have more attenuation than the red one. The seismic responses coincide with the sensitivity of petrophysical parameters to Q_p and V_p. We could effectively quantify these sensitivities in a post-migration analysis manner. In return, we could use the seismic response to predict the petrophysical model. This will be our future work.

4. Conclusions

In this study, we integrated the reservoir modeling, rock physics model and seismic modeling to characterize the properties of the saline aquifer and examine these properties to the CO_2 storage. We concentrated on four parameters—permeability, porosity, formation pressure, and temperature—to analyse the petrophysical and seismic response of CO_2. The following conclusions can be drawn.

(1) We conducted sensitivity analysis using both homogeneous and heterogeneous models. The homogeneous models consisted of a simple model with flat layers and a more realistic model with anticline and faults cutting through. The heterogeneous models consisted of random models for case 1 and case 2. Each model is generated by the SGSIM algorithm with the same variogram model. Both homogeneous and heterogeneous models produce consistent conclusions. The results suggest that an increase in temperature and $\log(K_h)$ leads to increase CO_2 saturation, while porosity and formation pressure decreases.
(2) Regarding the sensitivity analysis, we individually perturbed each parameter to calculate how their variations affected the CO_2 saturation. We found that permeability is the primary factor influencing changes in CO_2 saturation among these four parameters. This finding remains consistent for both homogeneous and heterogeneous models. Therefore, when exploring the sensitivity of CO_2 saturation to Q_p and V_p, we only analysed a simple model with flat layers in the homogeneous model. The results indicate that porosity is a significant factor affecting Q_p and V_p. It is observed that an increase in porosity leads to an increase in both Q_p and V_p, contrary to observations in gas reservoirs.
(3) The viscoacoustic wave equation is applied for seismic forward modeling and reverse time migration without compensation. The seismic simulation results reveal substantial variations in seismic response to different parameters. We provided spectral analysis for these observations, which can effectively quantify the variation in the sensitivity, potentially aiding petrophysical model estimation in the future.

Data availability statement

This study is made possible by the publicly shared the Johansen Dataset: https://co2datashare.org/dataset/the-johansen-dataset. The synthetic models are not open source yet.

CRediT authorship contribution statement

Yan-Jiao Dong: Writing – review & editing, Writing – original draft, Software, Methodology, Conceptualization. **Yi Shen:** Writing – review & editing, Supervision, Project administration, Methodology, Data curation, Conceptualization. **Kai Guo:** Project administration, Funding acquisition. **Xiao-Qin Wu:** Validation, Software. **Qiang Mao:** Validation, Methodology. **Wen-Yue Sun:** Software, Formal analysis. **Zhi-Qiang Wang:** Software.

Declaration of competing interest

The authors declare that they have no known competing financial interests or personal relationships that could have appeared to influence the work reported in this paper.

Acknowledgements

This study is supported by the State Key Laboratory of Offshore Oil and Gas Exploitation, Open Fund Project (No. CCL2023RCPS0162RQN) as the primary funding, National Natural Science Foundation of China (No. ZX20230400). The authors want to thank the GEET and SIIG in China University of Petroleum (East China) for financial support and discussions. Additionally, the authors are thankful for the support provided by Xiu-Chuan Liu and Tian-Yu Jia in the realm of seismic imaging. In particular, the authors would like to express special gratitude to CNOOC for granting permission to publish. Meanwhile, the authors also thank Norsk Hydro, Statoil (now Equinor) and Shell for their contributions to the Johansen Dataset.

Appendix A

Feasibility verification of the proposed simulation using the Johansen Dataset

We have chosen to validate the effectiveness of our method utilizing the Johansen formation, which features sparse sandstone conditions. The Johansen formation, located offshore the southwest coast of Norway, serves as a potential site for large-scale CO_2 storage. The dataset provided by https://co2datashare.org/dataset presents the CO_2 sequestration projects within the Johansen formation. The structure and injection well location of this dataset exhibit great similarity to our complex model.

Additionally, the Johansen Formation is situated approximately 2700 m below sea level, featuring a porosity range of 7.3%–31.4% and a permeability range spanning from 0.1 to 500 mD (Bergmo et al., 2009; Marashi, 2022). PVT (Pressure, volume, temperature) data is presented based on the characteristics of water and CO_2 at a steady temperature of 94 °C. The original pressure is recorded at 313.1 bar while at a true vertical depth of 3100 m. The injection strategy begins in 2014 and consists of 25 years of continuous CO_2 injection, followed by an additional 75 years of monitoring through shut-in wells. During the simulation, the annual injection volume of CO_2 is 1.5 Mt, with a CO_2 injection rate of 2091990 sm^3/day. The other parameter Settings for simulating CO_2 injection in the Johansen Formation in Eclipse 300 are consistent with the model we built in this paper, and the simulation results are shown in Fig. 20. Fig. 20 share same modeling results compared to the model we constructed in this paper, highlighting the effectiveness of the proposed method. After the injection of CO_2, the CO_2 plume in the reservoir grows in size and extends further over time. The simulation results are consistent with those presented in Sundal et al. (2015) for the basic case #A of the Johansen Formation local model. As a result, this example demonstrates the feasibility of our method for monitoring injected CO_2.

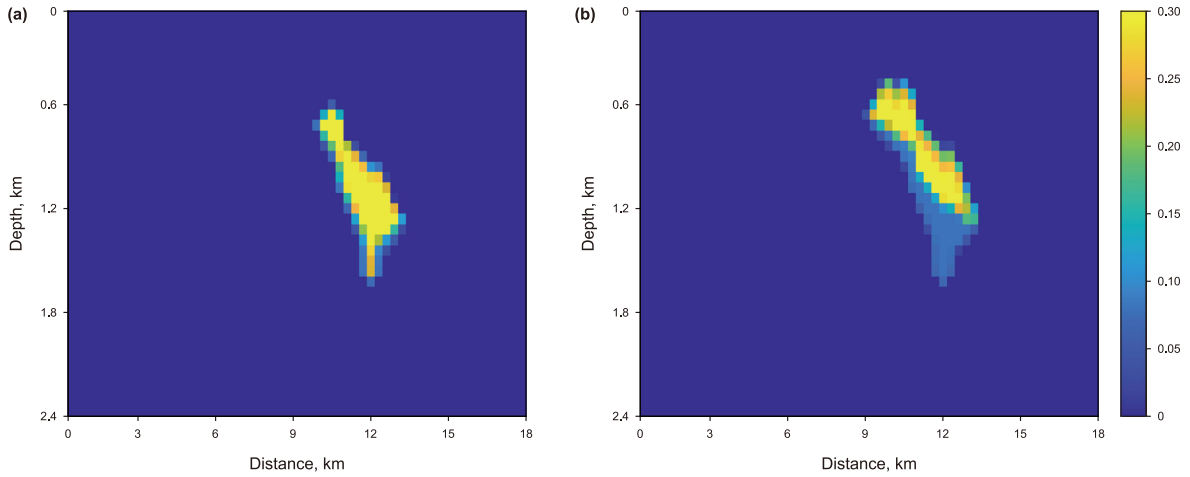

Fig. 20. Simulation results of the Johansen Formation: **(a)** CO_2 plume distribution over 25 years **(b)** CO_2 plume distribution over 100 years.

References

Ajo-Franklin, J., Peterson, J., Doetsch, J., et al., 2013. High-resolution characterization of a CO_2 plume using crosswell seismic tomography: cranfield, MS, USA. Int. J. Greenh. Gas Control 18, 497–509. https://doi.org/10.1016/j.ijggc.2012.12.018.

Al-Khdheeawi, E.A., Vialle, S., Barifcani, A., et al., 2017. Influence of injection well configuration and rock wettability on CO_2 plume behaviour and CO_2 trapping capacity in heterogeneous reservoirs. J. Nat. Gas Sci. Eng. 43, 190–206. https://doi.org/10.1016/j.jngse.2017.03.016.

Arts, R., Eiken, O., Chadwick, A., et al., 2004. Monitoring of CO_2 injected at Sleipner using time-lapse seismic data. Energy 29 (9–10), 1383–1392. https://doi.org/10.1016/j.energy.2004.03.072.

Bachu, S., 2001. Screening and ranking of hydrocarbon reservoirs for CO_2 storage in the Alberta Basin, Canada. In: US Department of Energy–National Energy Technology Laboratory, National Conference on Carbon Sequestration. https://api.semanticscholar.org/CorpusID:17042869.

Bachu, S., 2007. Carbon dioxide storage capacity in uneconomic coal beds in Alberta, Canada: Methodology, potential and site identification. Int. J. Greenh. Gas Control 1 (3), 374–385. https://doi.org/10.1016/S1750-5836(07)00070-9.

Bachu, S., Gunter, W., Perkins, E., 1994. Aquifer disposal of CO_2: hydrodynamic and mineral trapping. Energy Convers. Manag. 35 (4), 269–279. https://doi.org/10.1016/0196-8904(94)90060-4.

Barajas-Olalde, C., Mur, A., Adams, D.C., et al., 2021. Joint impedance and facies inversion of time-lapse seismic data for improving monitoring of CO_2 incidentally stored from CO_2 EOR. Int. J. Greenh. Gas Control 112, 103501. https://doi.org/10.1016/j.ijggc.2021.103501.

Bergmo, P.S., Lindeberg, E., Riis, F., et al., 2009. Exploring geological storage sites for CO_2 from Norwegian gas power plants: Johansen formation. Energy Proc. 1 (1), 2945–2952. https://doi.org/10.1016/j.egypro.2009.02.070.

Bourne, S., Crouch, S., Smith, M., 2014. A risk-based framework for measurement, monitoring and verification of the Quest CCS Project, Alberta, Canada. Int. J. Greenh. Gas Control 26, 109–126. https://doi.org/10.1016/j.ijggc.2014.04.026.

Carcione, J., Cavallini, F., Mainardi, F., 2002. Time-domain seismic modeling of constant Q-wave propagation using fractional derivatives. Pure Appl. Geophys. 159, 1719–1736. https://ricerca.ogs.it/handle/20.500.14083/16479.

Carcione, J.M., Kosloff, D., Kosloff, R., 1988. Viscoacoustic wave propagation simulation in the earth. Geophysics 53 (6), 769–777. https://doi.org/10.1190/1.1442512.

Carcione, J.M., Picotti, S., Gei, D., et al., 2006. Physics and seismic modeling for monitoring CO_2 storage. Pure Appl. Geophys. 163, 175–207. https://doi.org/10.1007/s00024-005-0002-1.

Chadwick, R., Williams, G., Falcon-Suarez, I., 2019. Forensic mapping of seismic velocity heterogeneity in a CO_2 layer at the Sleipner CO_2 storage operation, North Sea, using time-lapse seismics. Int. J. Greenh. Gas Control 90, 102793. https://doi.org/10.1016/j.ijggc.2019.102793.

Couëslan, M.L., Butsch, R., Will, R., et al., 2014. Integrated reservoir monitoring at the Illinois basin–decatur project. Energy Proc. 63, 2836–2847. https://doi.org/10.1016/j.egypro.2014.11.306.

Dai, Z., Stauffer, P.H., Carey, J.W., et al., 2014. Pre-site characterization risk analysis for commercial-scale carbon sequestration. Environ. Sci. Technol. 48 (7), 3908–3915. https://doi.org/10.1021/es405468p.

Davis, T.L., Terrell, M.J., Benson, R.D., et al., 2003. Multicomponent seismic characterization and monitoring of the CO_2 flood at Weyburn Field, Saskatchewan. Lead. Edge 22 (7), 696–697. https://doi.org/10.1190/1.1599699.

Eiken, O., Ringrose, P., Hermanrud, C., et al., 2011. Lessons learned from 14 years of CCS operations: sleipner, in Salah and Snøhvit. Energy Proc. 4, 5541–5548. https://doi.org/10.1016/j.egypro.2011.02.541.

Gershenzon, N.I., Ritzi Jr, R.W., Dominic, D.F., et al., 2015. Influence of small-scale fluvial architecture on CO_2 trapping processes in deep brine reservoirs. Water Resour. Res. 51 (10), 8240–8256. https://doi.org/10.1002/2015WR017638.

Iglauer, S., Al-Yaseri, A.Z., Rezaee, R., et al., 2015. CO_2 wettability of caprocks: implications for structural storage capacity and containment security. Geophys. Res. Lett. 42 (21), 9279–9284. https://doi.org/10.1002/2015GL065787.

Jin, L., Barajas-Olalde, C., Bosshart, N., 2021. Application of CO_2 injection monitoring techniques for CO_2 EOR and associated geologic storage. Proceedings of the 15th Greenhouse Gas Control Technologies Conference, pp. 15–18. https://doi.org/10.2139/ssrn.3812730.

Johnston, D.H., 2013. Practical applications of time-lapse seismic data. Society of Exploration Geophysicists. https://doi.org/10.1190/1.9781560803126.

Kazemeini, S.H., Juhlin, C., Fomel, S., 2010. Monitoring CO_2 response on surface seismic data; a rock physics and seismic modeling feasibility study at the CO_2 sequestration site, Ketzin, Germany. J. Appl. Geophys. 71 (4), 109–124. https://doi.org/10.1016/j.jappgeo.2010.05.004.

Kjartansson, E., 1979. Constant Q-wave propagation and attenuation. J. Geophys. Res. Solid Earth 84, 4737–4748. https://doi.org/10.1029/JB084iB09p04737.

Kramers, H.A., 1940. Brownian motion in a field of force and the diffusion model of chemical reactions. Physica 7 (4), 284–304. https://doi.org/10.1016/S0031-8914(40)90098-2.

Lackner, K.S., 2003. A guide to CO_2 sequestration. Science 300 (5626), 1677–1678. https://doi.org/10.1126/science.1079033.

Lazaratos, S.K., Marion, B.P., 1997. Crosswell seismic imaging of reservoir changes caused by CO_2 injection. Lead. Edge 16 (9), 1300–1308. https://doi.org/10.1190/1.1437788.

Leong, Z.X., Zhu, T., Sun, A.Y., 2022. Estimating CO_2 saturation maps fromseismic data using deep convolutional neural networks. Second International Meeting for Applied Geoscience & Energy, pp. 510–514. https://doi.org/10.1190/image2022-3746727.1.

Li, B., Li, Y.E., 2021. Neural network-based CO_2 interpretation from 4D sleipner seismic images. J. Geophys. Res. Solid Earth 126 (12), e2021JB022524. https://doi.org/10.1029/2021JB022524.

Lumley, D., 2010. 4D seismic monitoring of CO_2 sequestration. Lead. Edge 29 (2), 150–155. https://doi.org/10.1190/1.3304817.

Mahyapour, R., Mahmoodpour, S., Singh, M., 2022. Effect of permeability heterogeneity on the dissolution process during carbon dioxide sequestration in saline aquifers: two-and three-dimensional structures. Geomechanics and Geophysics for Geo-Energy and Geo-Resources 8 (2), 70. https://doi.org/10.1007/s40948-022-00377-3.

Marashi, S.V., 2022. Northern Lights Project: Aurora Model Investigation with Sensitivity Studies and Using Different Simulation Methods. Master thesis, NTNU. https://hdl.handle.net/11250/2992379.

Mathieson, A., Midgley, J., Dodds, K., et al., 2010. CO_2 sequestration monitoring and verification technologies applied at Krechba, Algeria. Lead. Edge 29 (2), 216–222. https://doi.org/10.1190/1.3304827.

Mavko, G., Chan, C., Mukerji, T., 1995. Fluid substitution: estimating changes in Vp without knowing vs. Geophysics 60 (6), 1750–1755. https://doi.org/10.1190/1.1443908.

Mavko, G., Mukerji, T., Dvorkin, J., 2009. The Rock Physics Handbook. Cambridge university press. https://doi.org/10.1017/CBO9780511626753.

Metz, B., Davidson, O., De Coninck, H.C., et al., 2005. IPCC Special Report on Carbon Dioxide Capture and Storage. Cambridge University Press, Cambridge. https://repository.ubn.ru.nl/handle/2066/230961.

Mualem, Y., 1976. A new model for predicting the hydraulic conductivity of unsaturated porous media. Water Resour. Res. 12 (3), 513–522. https://doi.org/10.1029/WR012i003p00513.

Mur, A., Barajas-Olalde, C., Adams, D.C., et al., 2020. Integrated simulation to seismic and seismic reservoir characterization in a CO_2 EOR monitoring application.

Lead. Edge 39 (9), 668–678. https://doi.org/10.1190/tle39090668.1.
Orlic, B., 2016. Geomechanical effects of CO_2 storage in depleted gas reservoirs in The Netherlands: inferences from feasibility studies and comparison with aquifer storage. J. Rock Mech. Geotech. Eng. 8 (6), 846–859. https://doi.org/10.1016/j.jrmge.2016.07.003.
Perera, M.S.A., Gamage, R.P., Rathnaweera, T.D., et al., 2016. A review of CO_2-enhanced oil recovery with a simulated sensitivity analysis. Energies 9 (7), 481. https://doi.org/10.3390/en9070481.
Perera, M.S.A., Ranjith, P., Choi, S., et al., 2012. Investigation of temperature effect on permeability of naturally fractured black coal for carbon dioxide movement: an experimental and numerical study. Fuel 94, 596–605. https://doi.org/10.1016/j.fuel.2011.10.026.
Raza, A., Gholami, R., Rezaee, R., et al., 2018. CO_2 storage in depleted gas reservoirs: a study on the effect of residual gas saturation. Petroleum 4 (1), 95–107. https://doi.org/10.1016/j.petlm.2017.05.005.
Remy, N., Boucher, A., Wu, J., 2009. Applied Geostatistics with SGeMS: A User's Guide. Cambridge University Press. https://doi.org/10.1017/CBO9781139150019.
Rutqvist, J., Vasco, D.W., Myer, L., 2010. Coupled reservoir-geomechanical analysis of CO_2 injection and ground deformations at in Salah, Algeria. Int. J. Greenh. Gas Control 4 (2), 225–230. https://doi.org/10.1016/j.ijggc.2009.10.017.
Shen, Y., Biondi, B., Clapp, R., 2018a. Q-model building using one-way wave-equation migration Q analysis—Part 1: theory and synthetic test. Geophysics 83 (2), S93–S109. https://doi.org/10.1190/geo2016-0658.1.
Shen, Y., Biondi, B., Clapp, R., 2018b. Q-model building using one-way wave-equation migration Q analysis—Part 2: 3D field-data test. Geophysics 83 (2), S111–S126. https://doi.org/10.1190/geo2017-0032.1.
Shen, Y., Dvorkin, J., Li, Y., 2018c. Improving seismic Q_P estimation using rock-physics constraints. Geophysics 83 (3), MR187–MR198. https://doi.org/10.1190/geo2016-0665.1.
Sheng, H., Wu, X., Sun, X., et al., 2023. Deep learning for characterizing CO_2 migration in time-lapse seismic images. Fuel 336, 126806. https://doi.org/10.1016/j.fuel.2022.126806.
Sohal, M.A., Le Gallo, Y., Audigane, P., et al., 2021. Effect of geological heterogeneities on reservoir storage capacity and migration of CO_2 plume in a deep saline fractured carbonate aquifer. Int. J. Greenh. Gas Control 108, 103306. https://doi.org/10.1016/j.ijggc.2021.103306.
Sundal, A., Miri, R., Ravn, T., et al., 2015. Modelling CO_2 migration in aquifers; considering 3D seismic property data and the effect of site-typical depositional heterogeneities. Int. J. Greenh. Gas Control 39, 349–365. https://doi.org/10.1016/j.ijggc.2015.05.021.
Tanase, D., Tanaka, J., 2021. Progress of CO_2 injection and monitoring of the Tomakomai CCS demonstration project. In: Proceedings of the 15th Greenhouse Gas Control Technologies Conference, pp. 15–18. https://doi.org/10.2139/ssrn.3817073.
Tonn, R., 1991. The determination of the seismic quality factor Q from VSP data: A comparison of different computational methods. Geophys. Prospect. 39 (1), 1–27. https://doi.org/10.1111/j.1365-2478.1991.tb00298.x.
van Genuchten, M.T., 1980. A closed-form equation for predicting the hydraulic conductivity of unsaturated soils. Soil Sci. Soc. Am. J. 44 (5), 892–898. https://doi.org/10.2136/sssaj1980.03615995004400050002x.
Wainwright, H.M., Finsterle, S., Zhou, Q., et al., 2013. Modeling the performance of large-scale CO_2 storage systems: a comparison of different sensitivity analysis methods. Int. J. Greenh. Gas Control 17, 189–205. https://doi.org/10.1016/j.ijggc.2013.05.007.
White, D., 2013. Seismic characterization and time-lapse imaging during seven years of CO_2 flood in the Weyburn field, Saskatchewan, Canada. Int. J. Greenh. Gas Control 16, S78–S94. https://doi.org/10.1016/j.ijggc.2013.02.006.
Wiese, B., Nimtz, M., Klatt, M., et al., 2010. Sensitivities of injection rates for single well CO_2 injection into saline aquifers. Geochemistry 70, 165–172. https://doi.org/10.1016/j.chemer.2010.05.009.
Will, R., Bratton, T., Ampomah, W., et al., 2021. Time-lapse integration at FWU: fluids, rock physics, numerical model integration, and field data comparison. Energies 14 (17), 5476. https://doi.org/10.3390/en14175476.
Xiao, B., Jiang, T., Lu, B., et al., 2018. Sensitivity analysis and optimization of technological parameters during coupled liquid CO_2 hydraulic fracturing/huff and puff treatment in tight oil reservoirs. AAPG Annual Convention & Exhibition, Salt Lake City, Utah, USA. https://doi.org/10.1306/42280Xiao2018.
Xu, T., Apps, J.A., Pruess, K., 2004. Numerical simulation of CO_2 disposal by mineral trapping in deep aquifers. Appl. Geochem. 19 (6), 917–936. https://doi.org/10.1016/j.apgeochem.2003.11.003.
Zhu, C., Zhang, G., Lu, P., et al., 2015. Benchmark modeling of the Sleipner CO_2 plume: calibration to seismic data for the uppermost layer and model sensitivity analysis. Int. J. Greenh. Gas Control 43, 233–246. https://doi.org/10.1016/j.ijggc.2014.12.016.
Zhu, T., Ajo-Franklin, J.B., Daley, T.M., 2017. Spatiotemporal changes of seismic attenuation caused by injected CO_2 at the Frio-II pilot site, Dayton, TX, USA. J. Geophys. Res. Solid Earth 122 (9), 7156–7171. https://doi.org/10.1002/2017JB014164.
Zhu, T., Harris, J.M., 2014. Modeling acoustic wave propagation in heterogeneous attenuating media using decoupled fractional Laplacians. Geophysics 79 (3), T105–T116. https://doi.org/10.1190/geo2013-0245.1.